



TECHNISCHE
UNIVERSITÄT
WIEN
Vienna University of Technology



BACHELORARBEIT

Interaction of Random Discrete Dopants with Oxide Traps

ausgeführt am

Institut für Mikroelektronik

zum Zwecke der Erlangung des akademischen Grades eines

Bachelor of Science (BSc)

unter der Leitung von

A.o. Univ.-Prof. Dipl.-Ing. Dr.techn. Tibor Grasser

und

Dipl.-Ing. Michael Waltl

durch

Alexander Toifl

Matrikelnummer 1228803

Dürnstein 120

3601 Dürnstein

Wien, im Juni 2016

Alexander Toifl

Abstract

The advancing miniaturization of metal-oxide semiconductor field effect transistors (MOSFETs) requires a profound understanding of degradation mechanism from a microscopic point of view. The important phenomenon called bias temperature instability (BTI) associated with charge traps has already been addressed by the four-state NMP model. A further issue that becomes essential when approaching nanoscale devices is the stochastic nature of individual dopants (referred to as variability), which is considered using random discrete dopant (RDD) simulations. In this thesis the influence of RDD on the capture and emission times of individual defects described by the four-state NMP model is investigated.

By setting up a simulation work flow using the general purpose semiconductor device simulator Minimos-NT, more than 35,000 discrete dopant distributions on a pMOSFET are analyzed in order to guarantee statistical significance. The influence of RDD is quantified by developing a data processing algorithm called *lateral shift method* that measures effective gate voltage shifts in the emission/capture times characteristics calculated using the four-state NMP model and in the transfer characteristics. The calculated gate voltage shifts are induced by the dopants' variability and are analyzed for different dopant distributions.

The gate voltage shifts are determined by comparing the results of RDD simulations to a reference simulation without RDD. To study the macroscopic and microscopic impact of RDD on the device, drain current versus gate voltage ($I_d(V_g)$) and capture/emission times versus gate voltage ($\tau_{c,e}(V_g)$) characteristics are analyzed. The former is observed to be not affected by different trap positions and only weakly by doping concentration, whereas the latter is influenced by both. Furthermore, the gate voltage shifts calculated from $\tau_{c,e}(V_g)$ characteristics are found to change their probability distribution when doping concentration or trap positions are varied.

Contents

1	Introduction	1
1.1	Scope of this Thesis	1
1.2	Structure	1
2	Bias Temperature Instability	2
2.1	Macroscopic Phenomena and Definitions	2
2.2	Microscopic Mechanisms	3
2.3	Measurement of Capture and Emission Times using TDDS	5
3	Outline of Four-State NMP Model and Random Discrete Dopant Simulations	7
3.1	The Four-State NMP Model	7
3.1.1	Defect Modeling using Two States	7
3.1.2	Metastable States	7
3.1.3	Non-Radiative Multiphonon Transitions	7
3.1.4	The Complete Four-State NMP Model	8
3.2	Random Discrete Dopants	8
4	Simulation Data Analysis	11
4.1	Fitting Functions to Data Points and the Least Squares Problem	11
4.2	Determination of Lateral Shift between Series of Data Points	13
5	RDD and NMP Simulations	17
5.1	The PMOSFET Device Structure	17
5.2	Simulation Work Flow	18
5.2.1	Device Model Initialization using <code>gtsstructure</code>	19
5.2.2	Automated RDD and NMP Simulations	20
5.2.3	Post-Processing	21
5.2.4	ΔV_g Extraction	22
5.2.5	Statistical Analysis and Visualization	24
6	Results	26
6.1	Normal Trap at Fixed Position	26
6.1.1	Single Fixed Trap located at Center of Gate Oxide	27
6.1.2	Single Fixed Trap near the Source Side of the Channel	30
6.2	Influence of Trap Position	32
7	Summary and Outlook	34
A	Appendix	36
	References	38

1 Introduction

In microelectronics, the recently developed strongly miniaturized semiconductor devices with geometrical dimensions of several tens of nanometers cause a variety of issues to be tackled. The most important are **reliability** of a single device and **variability** of devices produced using the same fabrication process. Concerning reliability, the origins of a phenomenon called **bias temperature instability** (BTI), which is prevalent in metal-oxide-semiconductor field effect transistors (MOSFETs), are still controversially discussed. Apart from that, the term variability refers to the atomistic and therewith stochastic nature of semiconductor materials, an unavoidable consequence of the production process. In order to enable a profound understanding, it is beneficial to investigate the influence of device variability on BTI.

1.1 Scope of this Thesis

For both, reliability and variability, well-founded research in the field of simulation was carried out at the Institute for Microelectronics [1–3]¹. The reliability issue of bias temperature instability has been addressed by the so-called four-state NMP (non-radiative multi-phonon) model. This model is implemented in the semiconductor device simulator Minimos-NT and allows to explain the characteristic capture and emission times observed from single traps in MOSFETs' gate stacks. The target of this thesis is to study the impact of the stochastic nature (variability) of the dopant distribution on the four-state NMP model (reliability) by answering the following question: *In how far does the stochastic and atomistic nature of semiconductor materials influence the capture and emission times of single traps calculated using the four-state NMP model?*

1.2 Structure

To answer this central question, **Chapter 2** describes the fundamental phenomena associated with the term BTI, both from a macroscopic and a microscopic point of view. In **Chapter 3** the essentials of the four-state NMP model and the approach to simulate random discrete dopant (RDD) distributions are discussed. The quantification of the influence of variability on the capture and emission times calculated using the four-state NMP model requires a data processing algorithm (*lateral shift method*), which has been developed in the course of this work and is discussed in detail in **Chapter 4**. Variability simulations demand a sufficiently large number of individual simulation runs in order to enable statistical statements. Therefore, an elaborate work flow, which organizes the interaction between the general purpose device simulator Minimos-NT, data extraction and post-processing has to be set up. In **Chapter 5** the chosen implementation is presented in detail and finally in **Chapter 6** the results are discussed.

¹The given references are only a small selection of the multitude of publications.

2 Bias Temperature Instability

The performance of MOSFETs is affected by different mechanisms. In this section 'bias temperature instability' (BTI) is introduced and discussed in detail. Furthermore, the impact of BTI on the transistor operating behavior and the experimental characterization of BTI is presented.

2.1 Macroscopic Phenomena and Definitions

In MOSFETs defects located in the gate stack or at the interface between the conducting channel and the gate stack are responsible for non-ideal operational behavior. Macroscopically, a shift of different MOSFET parameters, e.g., transconductance, channel mobility and subthreshold slope is visible [3]. The phenomenon responsible for this non-ideal device behavior is called BTI. In particular, the MOSFETs' threshold voltage V_{th} is affected. Thus, the degradation of MOSFETs is often characterized using the **time dependent** threshold voltage shift $\Delta V_{th}(t)$ [4].

The inset of Fig. 1 shows the typical experimental setup, which illustrates the basic influence of BTI. The drain, source and bulk terminals are set to zero, while a negative gate voltage (negative stress, in this case $V_g = -2\text{ V}$) is applied. Fig. 1 illustrates the threshold voltage shift as a function of time for a stress and relaxation cycle recorded on a **large-area pMOSFET**. After the stress time of $t_s = 1000\text{ s}$ has elapsed a gate voltage near V_{th} is applied and the device recovers (relaxation process). It is clearly visible that the threshold voltage shift does not vanish, even after $1000\text{ s} \approx 0.27\text{ h}$ of recovery. This leads to the distinction of a **recoverable (relaxation)** and a **nonrecoverable (permanent)** component of BTI [5].

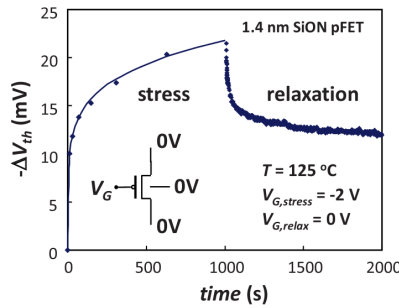


Fig. 1: Observed threshold voltage shift of a large-area pMOSFET after the device has been subjected to NBTI stress. The figure is taken from [5], Fig. 1.

The name bias temperature instability emphasizes the **strong temperature dependence** of device degeneration. Higher temperatures lead to intensified gate voltage shifts and therefore accelerated degradation [5]. BTI also occurs in nMOSFETs, where the gate is typically positively biased. This leads to a separation of the phenomenon BTI into negative BTI (**NBTI**) and positive BTI (**PBTI**). PBTI is observed when **positive** stress voltages are applied at the gate contact. NBTI corresponds to a **negatively** biased gate. For negatively biased pMOSFET the threshold voltage shift associated with NBTI is the most pronounced, as it is illustrated in Fig. 2 with measurement data from [6]. Even though minor degradation is visible on nMOSFETs (PBTI) as well, most investigations are on NBTI in pMOSFET devices, as carried out in Chapter 6.

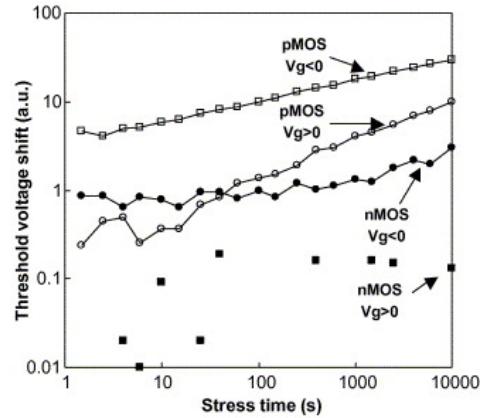


Fig. 2: Threshold voltage shift for different MOSFETs and stress biases, taken from [6], Figure 2. A significantly higher ΔV_{th} is achieved for pMOSFETs subjected to NBTI ($V_g < 0$, open squares) and PBTI ($V_g > 0$, open circles) stress. In contrast, nMOSFETs show less degradation for both NBTI (filled circles) and PBTI (filled squares).

2.2 Microscopic Mechanisms

From the microscopic point of view BTI is a consequence of charging and discharging of oxide defects and interface states², which exist due to structural imperfection. For classical MOSFET structures the silicon/silicon dioxide (Si/SiO₂) material system is used. An insulating oxide (SiO₂) is grown on the Si-substrate to form a thin layer. In modern transistors the insulating SiO₂ layer is thinner than 5 nm. The perfect SiO₂ structure is formed by tetrahedral cells where every Si atom is bonded to four adjacent oxygen (O) atoms.

Variations of the ideal atomic structure of SiO₂ give rise to the so-called **border states** (slow states). One possible defect configuration is the E' center³, where a silicon atom is only bonded to three adjacent oxygen atoms resulting in an unpaired electron. Fig. 3 schematically illustrates the defect configuration. During normal device operation such E' centers can capture a hole from the conducting channel, leading to an additional trapped charge inside the oxide layer [3].

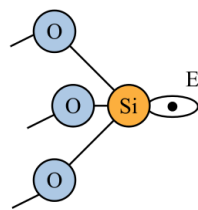


Fig. 3: The configuration of the E' center shows the three oxygen atoms bonded to a Si atom. The fourth Si bond remains unpaired. The illustration is taken from [3], Figure 3.7 a).

Nevertheless, defects located in the insulating oxide layer are not the only contributors to trapped charges. At the Si/SiO₂ interface the so-called **interface states** are present. These states are the consequence of an abrupt junction between Si and SiO₂ which are two materials with different lattices constants and thermal expansion coefficients. Analogously to border states, interface states can be possibly charged or discharged during device operation [1, 7]. In general, there are even further types of defects and charge traps whose microscopical details are still controversially discussed. In particular, for (trapped) oxide charge a phenomenological terminology has become established. Already in 1980 four oxide charge types were

²The term 'state' is used here in the quantum mechanical sense.

³As the microscopical details are still discussed, the E' center serves just as an exemplary illustration.

introduced [8]. NBTI is attributed to two of them, **interface trapped charge** and **oxide trapped charge** [4].⁴

The key mechanisms of trapped charge are the electron **capture** and **emission** process. The simplest way to model the defect transitions is to describe the defect by **two stable states**: neutral or positively/negatively charged. A defect is called **donor-like** when it can be positively charged, otherwise **acceptor-like** [1]. For NBTI studied in pMOSFETs donor-like defects are of importance as holes are the majority carriers in p-type channel transistors.

To characterize the trapped charges' influence on MOSFET operation the transition rates k , i.e., transition probability per unit time, are significant. Transition **probabilities** are considered, because of the **stochastic** nature of charge trapping. For the simple model the quantity $\tau = \frac{1}{k}$ can be interpreted as the transition **time constant**. The time constants are in general different for the charge capture and emission process, leading to the frequently used **capture** and **emission times**.

In case of charge capturing/emission a single charge carrier affects the threshold voltage in MOSFETs, because the quasi-electrostatics of the device changes. The impact of such a charging/discharging process varies for different device geometries. In Fig. 1 threshold voltage shift ΔV_{th} is illustrated for a **large area** device. As can be seen a continuous ΔV_{th} behavior is observed. For **nanoscale** devices (width \times length = 200 nm \times 200 nm or smaller), however, discrete threshold voltage shifts corresponding to single charge capture and emission events can be measured (Fig. 4 top). This arises from the fact that in nanoscale devices the number of defects is very small⁵, which allows to measure the influence of individual traps on ΔV_{th} . The time of a discrete voltage step to occur is referred to as the **emission time** τ_e . Another important parameter is the **capture time** τ_c . Profiting from the small number of traps present in the nanoscale devices the so-called *time dependent defect spectroscopy* (TDDS) has been introduced to study the charge capture/emission behavior of single traps [9, 10].

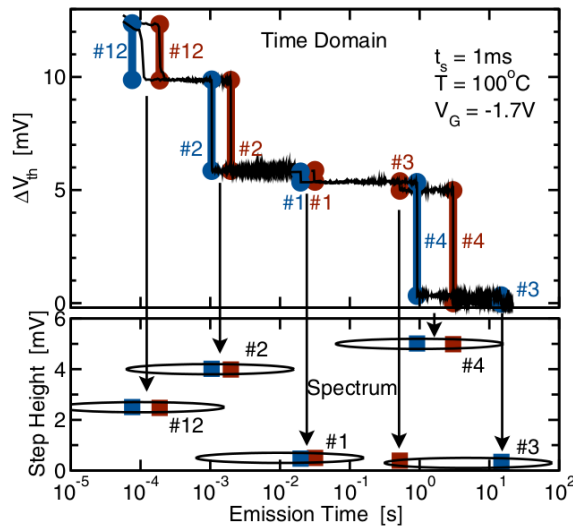


Fig. 4: Top: The recovery of nanoscale devices proceeds in discrete steps, i.e., the charge emission events of the single traps. **Bottom:** The step heights and emission times are collected in the step height versus emission time plane, called spectral map. The single emission events form clusters which are the fingerprints of single traps. Published in [10], Fig. 1.

⁴The remaining oxide charge types defined in [8] were oxide charge and mobile ionic charge.

⁵In modern devices we have a countable number with just a handful of defects [9].

2.3 Measurement of Capture and Emission Times using TDDS

Within the framework of TDDS the discrete threshold voltage shifts of single defects present in nanoscale devices are analyzed. An emission event of a defect results in a characteristic ΔV_{th} and a characteristic emission time τ_e , which is registered in a 2D histogram (referred to as *spectral map*, Fig. 4 bottom and Fig. 5). Thus, the spectral map characterizes the entirety of defects in the gate oxide which have been charged during the applied stress bias condition and get uncharged during recovery at the applied recovery bias condition at a certain temperature. To achieve a statistically relevant amount of data stress/recovery cycles are recorded 100 times and all emission events are collected in the resulting spectral map. The resulting spectral maps enable the identification of different traps with step different heights and emission times.

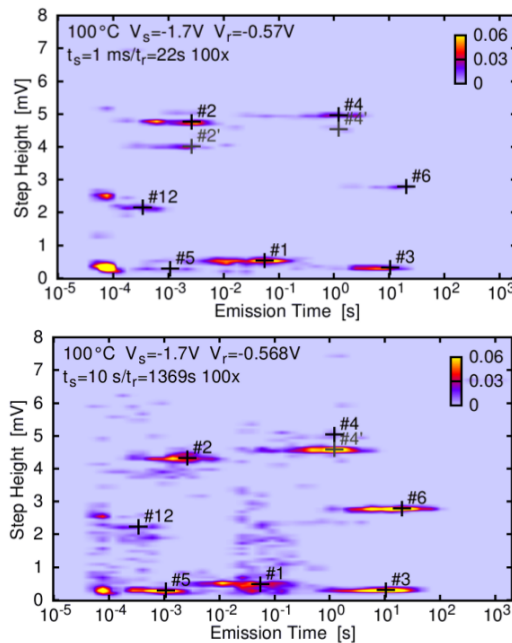


Fig. 5: Two spectral maps for different stress times of $t_s = 1$ ms (top) and $t_s = 10$ s (bottom). Quite noteworthy, with increasing stress times the intensity of the clusters increases. As the number of emission events is correlated to the cluster intensity it follows that with longer t_s the probability of a single defect to get charged during stress increases. The spectral maps are taken from [10], Fig. 2.

If a **single defect** is considered, the characteristic **emission time** τ_e can be directly calculated as the **mean value** of the emission times obtained from each individual trap. The **capture time** τ_c can be measured by increasing stress time and analyzing the consequentially increasing number of emission events [10].

The capture and emission times are characteristic parameters for the charging dynamics of single traps. Thus, their values directly influence device operation and degradation. To further describe the trapping kinetics the gate bias and temperature dependence of τ_c and τ_e is of utmost importance. Fig. 6 shows $\tau_{c,e}$ -characteristics extracted at a certain temperature from measurement data for the pMOSFET transistor considered in Chapter 5 and 6. It has to be noted that the investigated pMOSFET shows only **one** defect under the used stress and recovery conditions. The transition times are plotted logarithmically, indicating a strong sensitivity of capture times on gate bias over several decades in time, while emission times are practically bias independent. Such traps are called fixed (charge) traps, further details are discussed in Section 3.1.4.

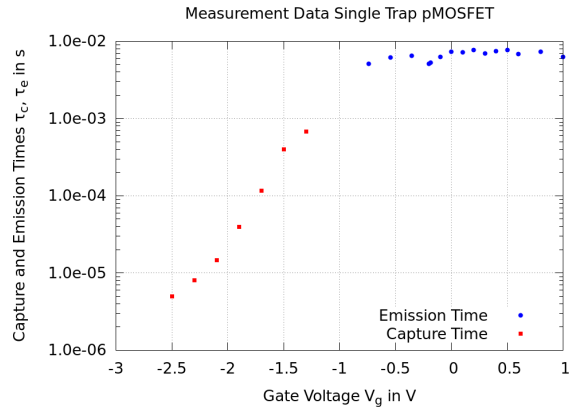


Fig. 6: Measured gate voltage dependence of transition times for a pMOSFET. Data was obtained using TDDS. The emission times appear to be independent of the recovery gate bias which is characteristic for so called fixed (charge) traps. In contrast, a strong stress bias dependence of the capture time is visible.

3 Outline of Four-State NMP Model and Random Discrete Dopant Simulations

In this thesis two individually developed models are employed: The first one is the four-state NMP model, which is used to describe the capture and emission times of single traps in the context of BTI. The second approach is the introduction of random discrete dopants. In this chapter the essentials of both models are discussed.

3.1 The Four-State NMP Model

3.1.1 Defect Modeling using Two States

To describe the characteristic capture and emission times of single traps an abstract approach to modeling is required. The different defect states and capture/emission processes discussed in Section 2.2 can be described using Markov processes [1]. Fig. 7 shows the simplest possible model. The defect is assumed to dwell in either a neutral or in a charged state.

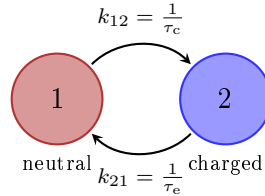


Fig. 7: Simple two-state transition diagram. The neutral defect state is assumed to be state 1, the charged defect state is identified with state 2. The transition rates are described by the time constants: capture time τ_c and emission time τ_e .

The parameters of such a model are the transitions rates between different states. The transition rate k_{AB} is the probability that a transition from state A to state B takes place during an unit time interval, typically given in units of s^{-1} . Using the simple process of Fig. 7, it can be shown that the transition rate can be alternatively characterized using the **expectation value** of the time point when the transition takes place [1]:

$$E(\tau_{AB}) = \frac{1}{k_{AB}}. \quad (1)$$

The capture and emission times, which are experimentally determined (Section 2.3), therefore, can be employed to characterize the charge trapping process. However, it is not surprising that model of such simplicity it not capable of describing all of BTI's main features [1,9].

3.1.2 Metastable States

A key characteristic of the so far described two-state model was its **stability** in both states. Stability refers to the defect's property to remain in this state even in equilibrium. On the contrary, experimental results and theoretical considerations concerning random telegraph noise and bias dependence of the capture/emission times suggest the existence of so-called *metastable states* [1, 10, 11]. Metastable states are not occupied in equilibrium, but are of utmost importance to correctly explain the bias dependence of transition rates.

3.1.3 Non-Radiative Multiphonon Transitions

The central feature of the four-state NMP model is the description of charge trapping not as a solely charge transfer but as a process that involves electron-phonon coupling. The transitions between stable and metastable states proceed in a **non-radiative** way. The energy that is interchanged during charge trapping is supplied via phonons (i.e., quantized collective

extinction of atoms or molecules). In the four-state NMP model **non-radiative** transitions, which involve phonons, are assumed to take place. Hence, the abbreviation NMP for non-radiative multiphonon (transition) emphasizes this distinctive conceptual element [1].

3.1.4 The Complete Four-State NMP Model

The four-state NMP model extends the simple description of Fig. 7 by adding two metastable states. One of the metastable states is considered to be electrically charged ($2'$), while the other one is neutral ($1'$). Fig. 8 illustrates the states and transitions of the complete four-state NMP model. The charge **capture** process takes place via the pathway $1 - 2' - 2$, therefore including as an intermediate stage the charged metastable state. For **emission** two transition pathways are possible, leading to a distinction between *switching traps* via the pathway $2 - 1' - 1$ and *fixed traps* via the pathway $2 - 2' - 1$. The first one is characterized by **bias-dependent emission times**, whereas the second one shows **no bias-dependence** of its emission times [1]. The trap shown in Fig. 6 displays bias independent emission times and thus is a fixed trap.

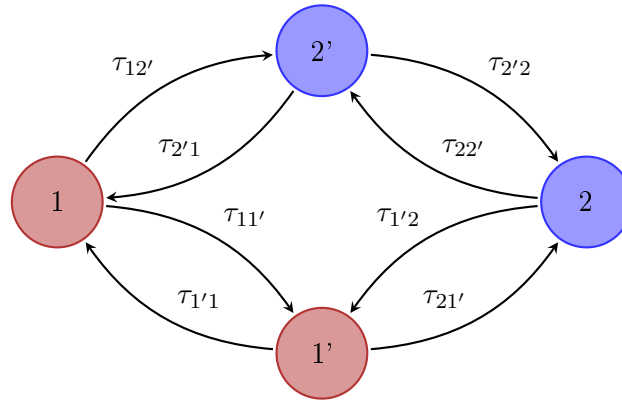


Fig. 8: The four-state NMP model's transition diagram consist of four states. (1) neutral stable, (2) charged stable, ($1'$) neutral metastable, ($2'$) charged metastable. Every transition is characterized by the corresponding transmission times. The diagram is reproduced from [9], Fig. 1.

The four-state NMP model's can correctly explain the transition times of single traps observed from TDDS experiments. For this a set of twelve parameters is available. On one hand device quantities like local electron concentration and electric potential are used, and on the other hand empirical parameters such as capture cross sections are involved. The carrier concentrations and potentials are provided by *drift-diffusion* based or quantum-corrected *density gradient* simulations. The necessity of empirical data is obvious as the four-state NMP model is not fully derived from first principles.

3.2 Random Discrete Dopants

Usually in device simulations doping concentration is considered as continuously distributed over the entire material. In reality, however, individual dopants are randomly distributed inside the bulk material. As the information on the position of the individual dopants is not available, a random distribution has to be assumed when performing variability simulations. For structures with geometrical dimensions in the μm -regime the typical donor and acceptor concentrations of more than 10^{17} cm^{-3} lead to very high numbers of individual dopants. To give an example, an acceptor concentration of 10^{17} cm^{-3} for a cubical segment with a common edge length of $1 \mu\text{m}$ results in 10^5 dopants located in this segment. Such a large number of dopants can be readily modeled by assuming a *continuous* distribution.

However, the persistent progress in device scaling in MOS-technology pushed the continuous treatment to a limit. The **nanoscale** SiGe high-k pMOSFET given in Fig. 9 has a channel doped with a donor concentration of $N_D = 10^{17} \text{ cm}^{-3}$ (central segment in Fig. 9). The drain and source regions show a high number of acceptors ($N_A = 6 \cdot 10^{19} \text{ cm}^{-3}$). The channel's geometrical dimensions are approximately $40 \text{ nm} \times 90 \text{ nm} \times 5 \text{ nm}$, resulting in an expected number of individual donors inside the channel of only 1.8. Thus, the quasi-electrostatic situation inside the channel is determined by one or two donor atoms which can obviously not be adequately modeled using a continuous distribution that is spread over the whole channel.

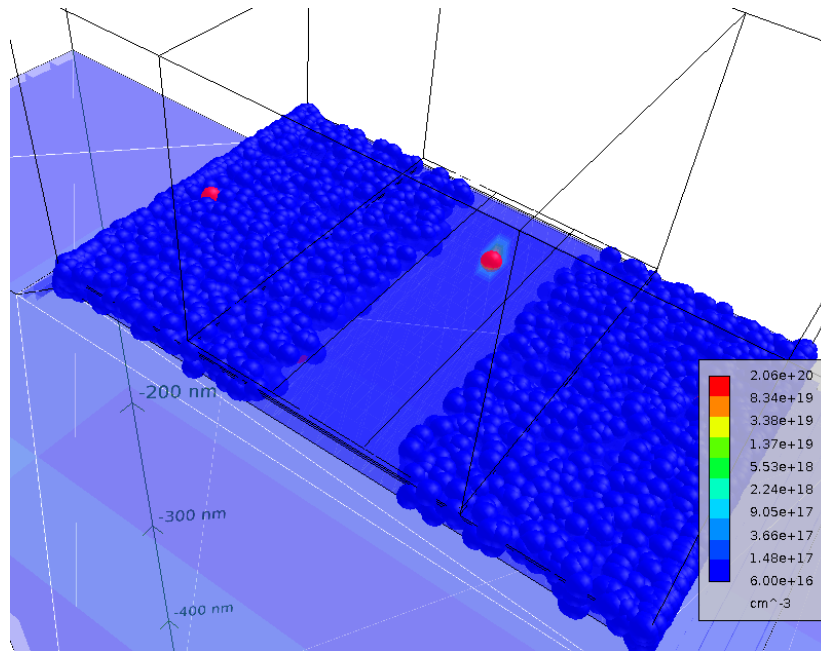


Fig. 9: Channel dopant distribution for a SiGe high-k pMOSFET. The colored (red: donors, blue: acceptors) spheres illustrate individual dopant positions. Surface coloring (with corresponding colorbar) indicates the consequential approximated continuous acceptor concentration.

The previous example shows an essential consequence of miniaturization. As a stochastic fluctuation of individual dopant positions between different devices is unavoidably introduced by process technology (doping process) the position and depth of acceptors and donors is a **stochastic** quantity and has a considerable impact on device functionality. This circumstance is termed **variability** and is of importance in semiconductor device fabrication. From the simulation point of view variability requires a statistical approach. It is not sufficient to simulate device properties for only one dopant distribution. A statistically sufficient number of devices that are macroscopically equivalent has to be taken into account. Thereby, the dopants' positions have to be generated randomly, giving rise to **random discrete dopant simulations**.

A natural approach to model discrete dopants within the **drift-diffusion** framework is to describe the corresponding electric potential as being sharply located (much like Dirac's delta function) and being assigned to the next grid point in the discretization scheme. Unfortunately, this leads to unphysically strong carrier localization [2]. However, inordinate localization can be avoided by splitting Coulomb potential in short-range and long-range parts and only considering the latter. The choice of cut-off points is critical here [12]. For the purpose of this thesis (see also Chapter 5) the density gradient (DG) model is used, as it has the ability to describe electric potential and consequent carrier concentrations in a very suitable way [2].

The varying positions of the RDD induce fluctuations in the quasi-electrostatics of the MOSFET. Considering transfer characteristics (drain current I_d versus gate voltage V_g) for different

dopant distributions, a shift along the gate voltage axis for different dopant distributions is visible. Fig. 10 exemplarily shows the transfer characteristics (on a logarithmic scale) for a pMOSFET. Compared to a continuous reference simulation (density gradient, no discrete dopants), the $I_d(V_g)$ characteristics originating from two different discrete dopant distributions clearly show a **lateral shift**. Macroscopically, this results in a threshold voltage shift ΔV_{th} . In Chapter 5 and 6 the quantity ΔV_{th} is used to quantify the influence of RDD on the capture and emission times calculated with the four-state NMP model.

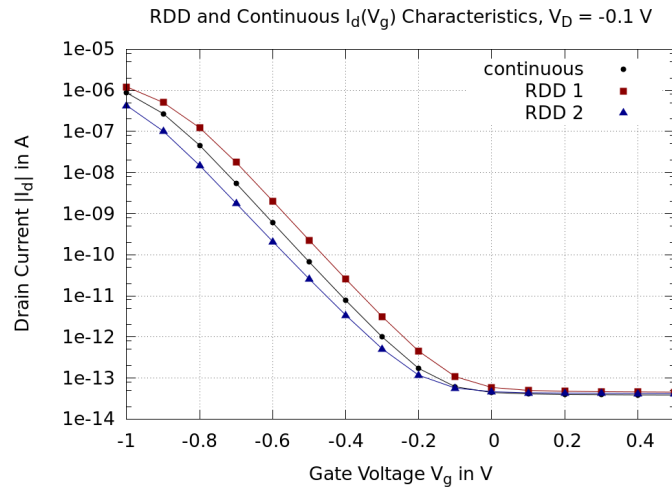


Fig. 10: $|I_d|(V_g)$ characteristics (transfer characteristics) for the pMOSFET shown in Fig. 14. The absolute value of drain current is plotted on a logarithmic scale over gate voltage. Two distinctive dopant distributions (RDD 1 and RDD 2) produce shifted versions of the transfer characteristics originating from continuous doping concentrations on the same device. The drain potential V_D is set to -0.1 V.

4 Simulation Data Analysis

As presented in Section 3.2, different discrete dopant distributions in a MOSFET lead to a lateral shift (i.e., shift along gate voltage axis) of the transfer characteristics $I_d(V_g)$. In order to enable statistical evaluations the **gate voltage shift** between two $I_d(V_g)$ data sets has to be examined. Because of its importance for following considerations (Chapter 5 and 6) this section's objective is to precisely formulate and the gate voltage shift problem and provide a solution. As it turns out, a crucial sub-problem is **curve fitting**, which one commonly encounters in data processing. Consequently, curve fitting is discussed first (Section 4.1). Afterwards, a method for extracting gate voltage shifts which is employed in this thesis is described (Section 4.2).

4.1 Fitting Functions to Data Points and the Least Squares Problem

First we consider a given set of experimentally obtained data, which is exemplarily shown in Fig. 11. For the subsequent investigation usually the qualitative behavior (linear, quadratic, ...) of the process that has created the data set is known, but the exact parameters are not.

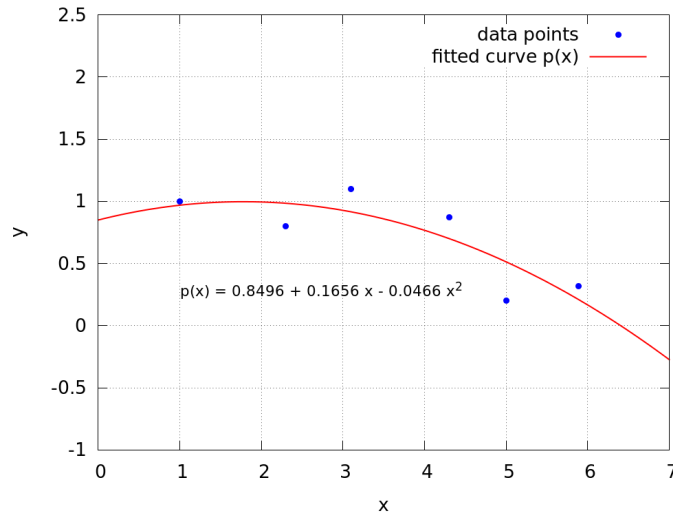


Fig. 11: A second-order polynomial (solid line) is fitted to a set of data points.

For the data given in Fig. 11 a quadratic functional relation between y- and x-values is considered. That means a second order polynomial $p(x) = a_0 + a_1x + a_2x^2$, that approximates the data points best has to be found. For polynomials of arbitrary degree the fitting problem can be defined as follows.

Definition 4.1 (*Data Fit Problem for Polynomials*)

Let $D = \{(x_0, y_0), (x_1, y_1), \dots, (x_{m-1}, y_{m-1})\} \subseteq \mathbb{R}^2$ be a set of m data points and $p(x) = a_0 + a_1x + \dots + a_{n-1}x^{n-1} = \sum_{i=0}^{n-1} a_i x^i$ a polynomial of degree $n - 1$. The problem to find the coefficients a_i , $i \in \{0, 1, \dots, n - 1\}$ in order that

$$y_j \approx p(x_j), j \in \{0, 1, \dots, n - 1\}$$

is called data fit problem for a polynomial of degree $n - 1$.

Definition 4.1 only clarifies that a good approximation is sought. Furthermore, a criterion is necessary to measure the quality of an approximation. The most common approach is using

the squared euclidean norm $\sum_{j=0}^{m-1} (y_j - p(x_j))^2$, which is requested to be minimized during the iterative fitting process. This approach leads to a special case of the general least squares problem, which is formulated in the following definition [13].

Definition 4.2 (*(Non-linear) Least Squares Problem*)

Find a local minimizer \mathbf{x}^* for

$$F(\mathbf{x}) = \sum_{j=0}^{m-1} f_j^2(\mathbf{x}),$$

with given functions $f_j : \mathbb{R}^n \rightarrow \mathbb{R}$, $j \in \{0, \dots, m-1\}$ and $m \geq n$.

The function $F : \mathbb{R}^n \rightarrow \mathbb{R}$ is called *cost function* or *score function*. It is important to note that a **local** minimizer and not a **global** minimizer is searched. These are defined as follows. [13]

Definition 4.3 (*Global and Local Minimizers*)

Let $F : \mathbb{R}^n \rightarrow \mathbb{R}$ be the cost function of a minimization problem.

$$\mathbf{x}_g = \arg \min_{\mathbf{x} \in \mathbb{R}^n} \{F(\mathbf{x})\}$$

is called **global minimizer** and

$$F(\mathbf{x}^*) \leq F(\mathbf{x}) \text{ for } \|\mathbf{x} - \mathbf{x}^*\| < \delta$$

with small $\delta > 0$ is called **local minimizer**. $\|\cdot\|$ denotes euclidean norm.

In general, the global minimizer is difficult to find using numerical techniques. This is the reason why the least squares problem (definition 4.2) only requires a **local** minimum of the cost function. The search for a local minimum, on the other side, permits algorithms to be restricted to work inside a certain finite region (determined by δ).

For the data fit problem, definitions 4.1 and 4.2 imply that $f_j = y_j - p(x_j)$. The vector to minimize \mathbf{x} in terms of the cost function $F(\mathbf{x})$ is in this case a vector containing the polynomial's coefficients, $\mathbf{a} = [a_0, a_1, \dots, a_{n-1}]^T$. The data fit problem for polynomials is actually a **linear** least squares problem, as can be seen by expressing the cost function in vector/matrix notation

$$\sum_{j=0}^{m-1} (y_j - p(x_j))^2 = \|\mathbf{y} - \mathbf{p}\|^2 = \|\mathbf{y} - \mathbf{X}\mathbf{a}\|^2, \quad (2)$$

where

$$\mathbf{p} = \begin{bmatrix} p(x_0) \\ p(x_1) \\ \vdots \\ p(x_{m-1}) \end{bmatrix} \quad (3)$$

and

$$\mathbf{X} = \begin{bmatrix} 1 & x_0 & x_0^2 & \dots & x_0^{n-1} \\ 1 & x_1 & x_1^2 & \dots & x_1^{n-1} \\ \vdots & \vdots & \vdots & \ddots & \vdots \\ 1 & x_{m-1} & x_{m-1}^2 & \dots & x_{m-1}^{n-1} \end{bmatrix} \quad (4)$$

is a **constant** *Vandemonde* matrix [14]. Consequently, $\mathbf{p} = \mathbf{X}\mathbf{a}$ is a vector with entries formed of *linear combinations* of $p(x_0), p(x_1), \dots, p(x_{m-1})$, giving rise to a **linear** least square problem.

To solve this linear equation, specialized numerical methods and also an analytical solution exist. Nevertheless, algorithms for **non-linear** least squares problems have been developed as well. The most important is the *Levenberg-Marquardt (LM) algorithm*, which is based on the *Gauss-Newton method* [13, 15]. The LM algorithm is widely used in plotting and optimization software for curve fitting. For example, the solid line in Fig. 11 is a quadratic polynomial whose coefficients have been calculated using `gnuplot`, which uses the LM method itself [16].

4.2 Determination of Lateral Shift between Series of Data Points

After defining the data fit problem in the previous section, the algorithm used to extract gate voltage shifts is presented. In the following the presented procedure is called *lateral shift method*. A central aspect is the satisfaction of the following prerequisite.

Prerequisite

Let $R = \{(x_0, y_{0,r}), (x_1, y_{1,r}), \dots, (x_{m-1}, y_{m-1,r})\} \subseteq \mathbb{R}^2$ be the **reference set** of m data points and $D = \{(x_0, y_0), (x_1, y_1), \dots, (x_{m-1}, y_{m-1})\} \subseteq \mathbb{R}^2$ be the **considered set** of m data points. The *lateral shift method* is only applicable if D defines a continuous function $\hat{y}(x)$ that is **approximately a shifted version** of the reference function $\hat{y}_r(x)$ (determined by R), i.e.,

$$\exists h \in \mathbb{R} \text{ such that } \hat{y}(x_i - h) \approx \hat{y}_r(x_i) \quad \forall i \in \{0, 1, \dots, m-1\}.$$

Fig. 12 shows the data points for the considered data set (points) and the reference data set (triangles). The discrete points can be interpreted as individual "measurement data points" of an underlying continuous function (solid lines). Obviously, the two functions are not just shifted versions of each other in a global sense. Especially around $x = -1$ and $x = 0$ the shape of the function changes. Consequently, an interval (e.g., in the underlying case $x \in [-0.8, -0.3]$) has to be defined for the lateral shift method to be applied.

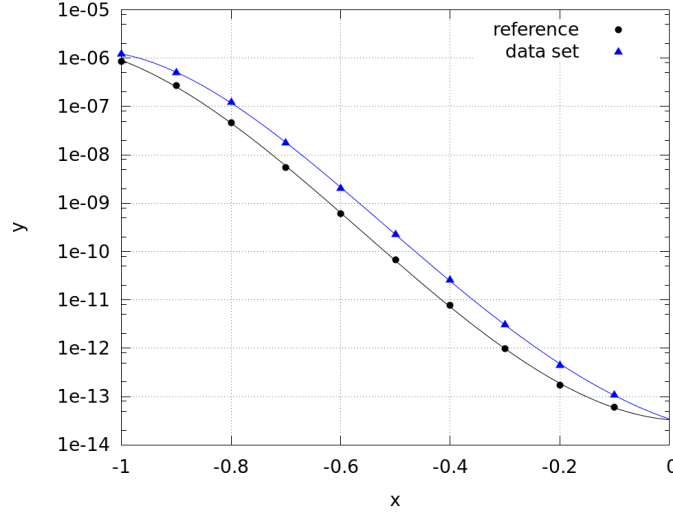


Fig. 12: Reference (triangles) and considered data set (points). The solid lines are the result of fourth-order polynomials fitted to the corresponding data values. As the y-axis is scaled logarithmically, the polynomials' coefficients are determined by first taking the decadic logarithm of the y-values and then using the least squares method (logarithmic fitting). Within the interval $[-0.8, -0.3]$ the obtained continuous approximations can be considered to be shifted versions of each other.

The lateral shift method comprises of two steps:

1. Find the best continuous functions $\hat{y}_r(x)$ and $\hat{y}(x)$ that approximates the given data set.
2. Find the lateral shift h^* that transfers $\hat{y}(x)$ into $\hat{y}_r(x)$. In the ideal case $\hat{y}(x-h^*) = \hat{y}_r(x)$.

Step 1 can be realized using the polynomial approximation of Section 4.1. The continuous functions are then

$$\hat{y}(x) = p_1(x) = \sum_{i=0}^{n-1} a_i x^i \quad \text{and} \quad \hat{y}_r(x) = p_2(x) = \sum_{i=0}^{n-1} b_i x^i. \quad (5)$$

The polynomials' degrees should be equal and the polynomial approximation should hold in a distinctive finite interval, i.e., $x \in [e_1, e_2]$.

Step 2 relies on an appropriate quantification of similarity between two functions. This is realized using a cost function $C_{a_i, b_i}(h)$ which depends on the approximate polynomial's coefficients a_i and b_i , but is a function of the data polynomial's lateral shift. Therefore, $C_{a_i, b_i}(h)$ is a real-valued one-dimensional function. The choice of the cost function provides some degrees of freedom but the following definition states one possibility.

Definition 4.4 (*Cost Function for the Lateral Shift Method*)

Let $E = \{e_1, e_1 + \frac{e_2 - e_1}{N}, e_1 + \frac{2(e_2 - e_1)}{N} + \dots + e_2\}$ be a linear subdivision (consisting of N values) of the interval $[e_1, e_2]$. The cost function $C_{a_i, b_i} : \mathbb{R} \rightarrow \mathbb{R}$ measures the similarity between the polynomial approximation of the reference data set $p_2(x) = \sum_{i=0}^{n-1} b_i x^i$ and the shifted version of the considered data's polynomial approximation $p_1(x) = \sum_{i=0}^{n-1} a_i x^i$. (The shift is quantified by $h \in \mathbb{R}$.) It is defined as

$$C_{a_i, b_i}(h) = \sum_{x_j \in E} (p_2(x_j) - p_1(x_j - h))^2.$$

$C_{a_i, b_i}(h)$ satisfies the necessary condition that it yields zero if two ideal replicas are compared.⁶ The cost function now enables a rigid definition of the lateral shift problem.

Definition 4.5 (*Lateral Shift Problem*)

With the cost function C_{a_i, b_i} from definition 4.4 the best lateral shift h^* is given by

$$h^* = \arg \min_{h \in \mathbb{R}} C_{a_i, b_i} = \arg \min_{h \in \mathbb{R}} \sum_{x_j \in E} (p_2(x_j) - p_1(x_j - h))^2.$$

In Section 4.1 it was pointed out that a global minimizer is numerically difficult to find. Therefore, a practical requirement for a cost function is to have a *local* minimum at the function argument of global minimum. In this case the global minimum is a local minimum as well. If this prerequisite is satisfied a weaker but more practical formulation can be given using the term *local minimizer* of definition 4.3.

Definition 4.6 (*Weaker Formulation of the Lateral Shift Problem*)

Find a local minimizer for

$$C_{a_i, b_i}(h) = \sum_{x_j \in E} (p_2(x_j) - p_1(x_j - h))^2.$$

with the cost function $C_{a_i, b_i}(h)$ given in definition 4.4.

Therewith, the lateral shift problem reduces to the following task: find the **local minimum of the real-valued scalar cost function**. Because of the scalar nature, basic algorithms as *golden section search (GSS)* which draws upon the same idea as *binary search algorithm* can be used [17]. GSS works on a predefined interval und assumes **unimodality**, i.e., only one minimum inside a certain interval. Additionally, there are iterative algorithms which are actually designed for multi-dimensional functions available. One example is the *Nelder Mead (NM) algorithm* [18], which requires an initial guess in order to start the iteration.

Fig. 13 exemplarily shows the cost function (left) for two data sets (right). It is clearly visible that the global minimum at $h_1 \approx -0.03$ is at also a local minimum. Nonetheless, a second local minimum at $h_2 \approx -1$ exists. This is very unpleasant for finding the global minimum numerically. Both above-mentioned algorithms (*GSS* and *NM*) can yield $h_2 \approx -1$ when either the interval or initial guess are close to h_2 , e.g., starting interval $[-2, -0.5]$ for *GSS* or -1.5 as initial guess for *NM*. Therefore, multiple runs under different initial conditions and subsequent comparison of the function values are required.

⁶The cost function's zeroes (or global minima) can possibly be ambiguous. This is the case for periodic $p_1(x)$, $p_2(x)$.

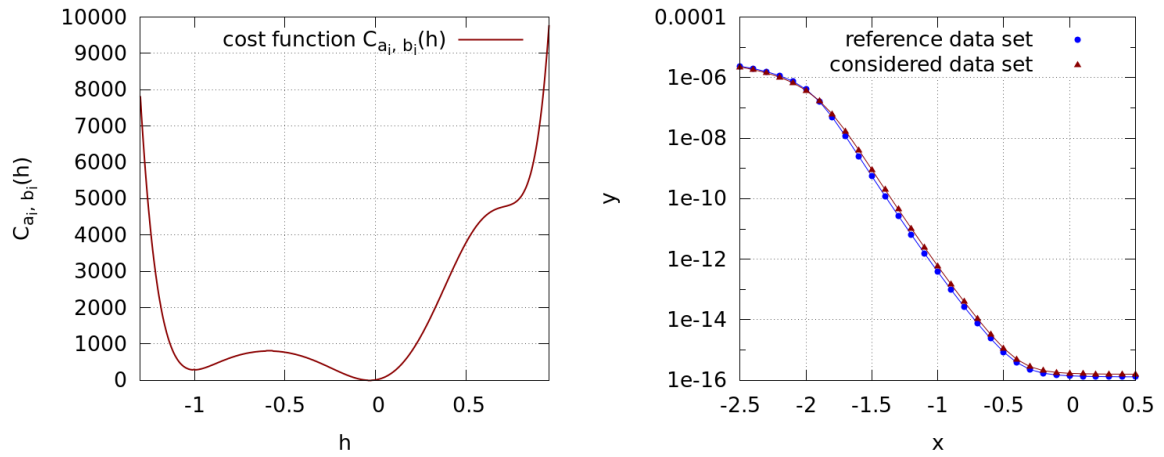


Fig. 13: Cost function (left) for the two data sets (right). The cost function has two local minima at $h_1 \approx -0.03$ and $h_2 \approx -1$, but only h_1 corresponds to an optimum shift h^* as it is the global minimum as well. Even at $h_1 \approx -0.03$ the cost function is non-zero, because $C_{a_i, b_i}(-0.03) \approx 0.6$.

5 RDD and NMP Simulations

The main task of this thesis is to implement a work flow to study the impact of different positions of dopant atoms on the capture and emission times calculated by the four-state NMP model. Both, the four-state NMP model and the RDD approach is implemented in the general purpose semiconductor device simulator Minimos-NT [19]. Thus, all simulations are carried through using this particular simulator. Around Minimos-NT a framework of different tools that enable device generation, results analysis and visualization is steadily developed by *Global TCAD Solutions* [20]. For the purpose of this thesis the device generation tool `gtsstructure`, the visualization tool `gtsvision` and the auxiliary tool `gtsinfo` are used inside a work flow that is described in this section [21]. In order to realize the required file management and mathematical calculations four Python [22] scripts are implemented. The following discussion starts from the creation of a pMOSFET device structure and explains the necessary steps to be able to analyze the discrete dopants' influence on capture and emission times for a single trap.

5.1 The PMOSFET Device Structure

The pMOSFET structure which is considered throughout the following investigations is illustrated in Fig. 14, with geometrical dimensions of width \times length = 150 nm \times 100 nm and a 2.4 nm thin SiO₂ insulation. As discussed in Section 2.2 for pMOSFETs with dimensions in the nano-meter regime the recovery proceeds in a discrete manner. Thus, the device is suitable for capture and emission time measurements of single defects using TDDS (Section 2.3). For the considered device capture and emission times have been extracted and the four-state NMP model parameter set was adjusted to reproduce the measured transition time characteristics (Section 3.1.4). The observed transition times are presented in Fig. 6.

To investigate the influence of discrete dopants on the calculated $\tau_{c,e}$ characteristics various random discrete dopant distributions are created with Minimos-NT. In Fig. 15 the position of the individual discrete dopants and the underlying continuous donor concentration is shown. It is important to emphasize that the discrete dopant distribution is actually generated based on the continuous donor and acceptor concentrations.

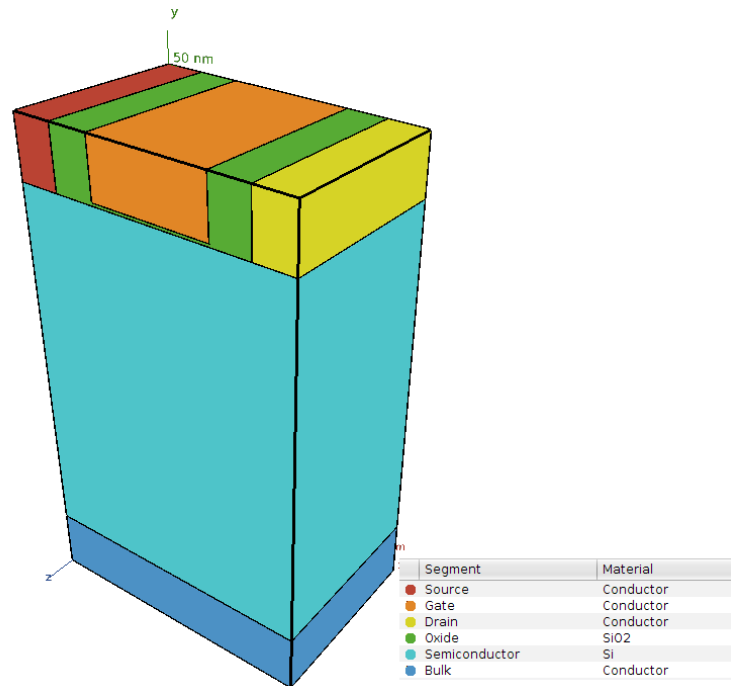


Fig. 14: Simulation structure for the pMOSFET structure. The colored segments of the pMOSFET schematically illustrate the materials which have been used for the transistor. All results presented in Chapter 6 were obtained by investigating this particular structure.

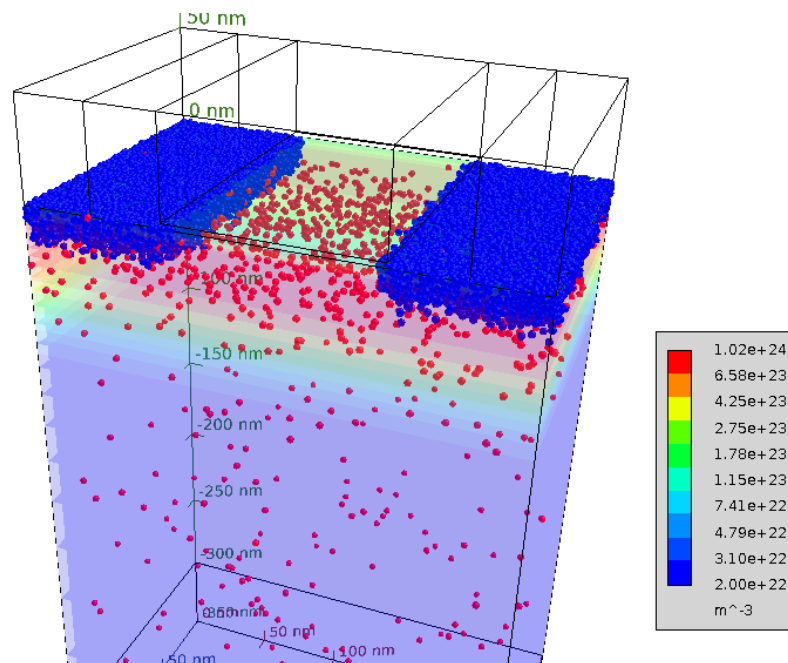


Fig. 15: Dopant distribution for the pMOSFET given in Fig. 14. The colored (red: donors, blue: acceptors) spheres illustrate individual dopant positions. The transparent coloring visualizes the continuous donor concentration which shows a steady decline towards bulk contact.

5.2 Simulation Work Flow

In the following the essential task of setting up a work flow that provides efficient simulations and post processing is presented. It has to be noted that for variability simulations (involving random discrete dopants) a large number of simulations is required to produce statistically relevant results. Therefore, a large number (e.g., 1,000 to 5,000) of individual discrete dopant

distributions has to be considered, leading to long simulation times. Apart from the device simulations performed with Minimos-NT, post processing, data acquisition and visualisation with a large dataset give rise to a variety of challenges.

The conceptual work flow, which has been constructed during this work, is depicted in Fig. 16. It can be separated into five subsequent tasks:

1. Device model initialization (block `gtsstructure` in Fig. 16)
2. Automated RDD and NMP simulations for 1,000 up to 5,000 dopant distributions (`dVthSim`)
3. Post processing to extract transition times, drain currents and gate voltages (`processDevice`)
4. ΔV_g extraction using the approach of Chapter 4 (`deltaVgExtraction`)
5. Statistical analysis and visualization (`batchStats`)

The following sections individually discuss the approaches to solve these tasks.

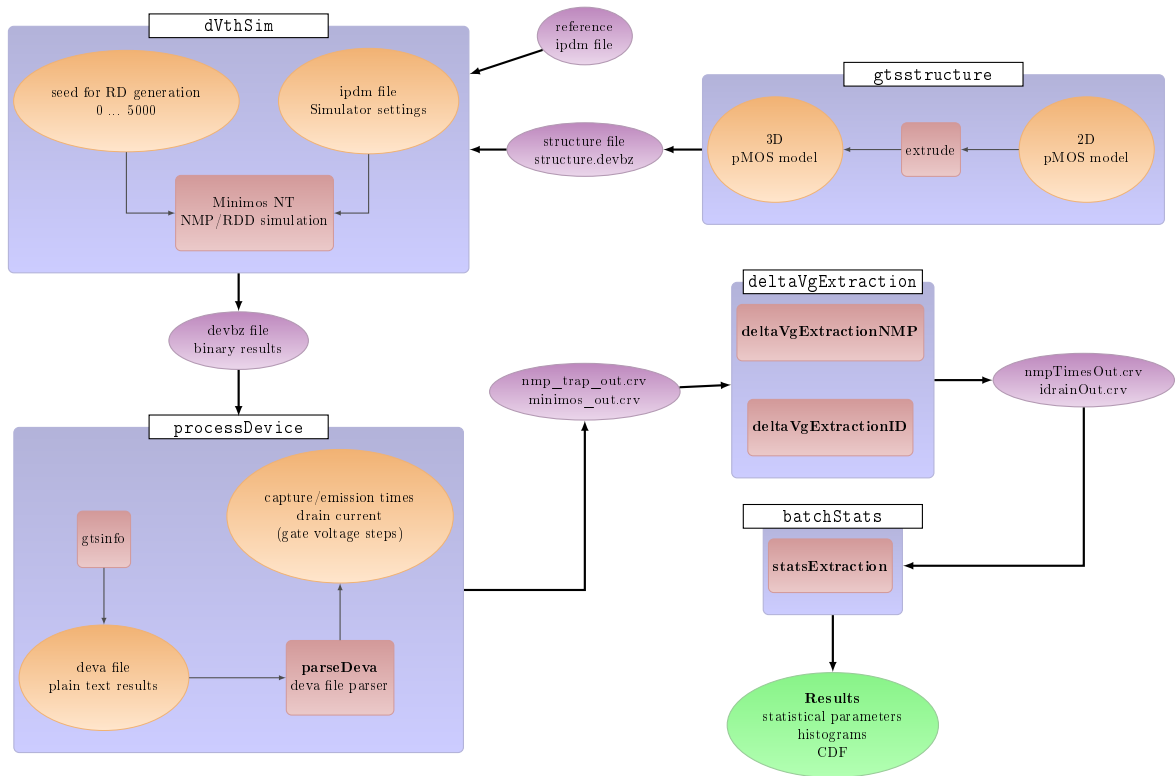


Fig. 16: The presented work flow which was implemented during this thesis. The **Elliptical nodes** illustrate files or objects that serve as input / output files of processes (**rectangular nodes**). The larger (outer) nodes with blue background depict the main subtasks explained in sections 5.2.1 to 5.2.5. The scripts which were developed within this thesis are **printed in bold**. Aside from `gtsstructure`, the outer nodes themselves illustrate the four main Python scripts.

5.2.1 Device Model Initialization using `gtsstructure`

Semiconductor device simulations are mostly performed using 2D device structures. The established process technology allows precise control of planar structure layering, supporting the reduction of the 3D devices to simplified 2D structures. Furthermore, a 2D model drastically saves computation time because only a reduced set of grid points is used.

By taking random dopant fluctuations into account a simple 2D structure model is not sufficient. Consequently, this thesis's work flow (the first part is given in Fig. 17) starts with the **extrusion** of the simplified 2D device structure (Fig. 18) to the 3D model which is shown in Fig. 14. The 2D model covers the geometry and the continuous doping distribution of the considered device. The extrusion is carried out using `gtsstructure`, resulting in an output file (`structure.devbz`), which contains the device's geometry and doping information (in binary format).

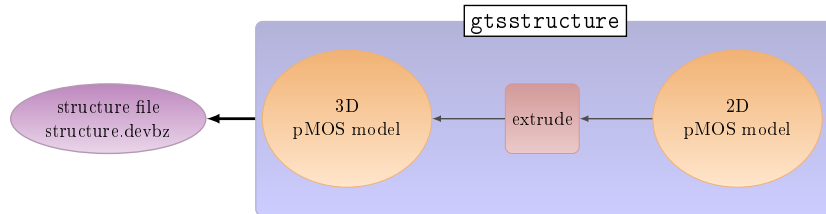


Fig. 17: Device initialization of the presented device, part of the entire work flow given in Fig. 16.

Furthermore, the segments which should feature **discrete dopants** have to be defined in the corresponding simulation setting file (`ipdm` file). In this particular case, only the substrate segment (called semiconductor in Fig. 14) is configured to consider a random discrete dopant distribution. Additionally, the **parameter set** for the **four-state NMP model** is defined in a **reference ipdm** file. The reference file acts as template configuration file which is altered during automatic simulations (see following section) in order to generate different dopant distributions.

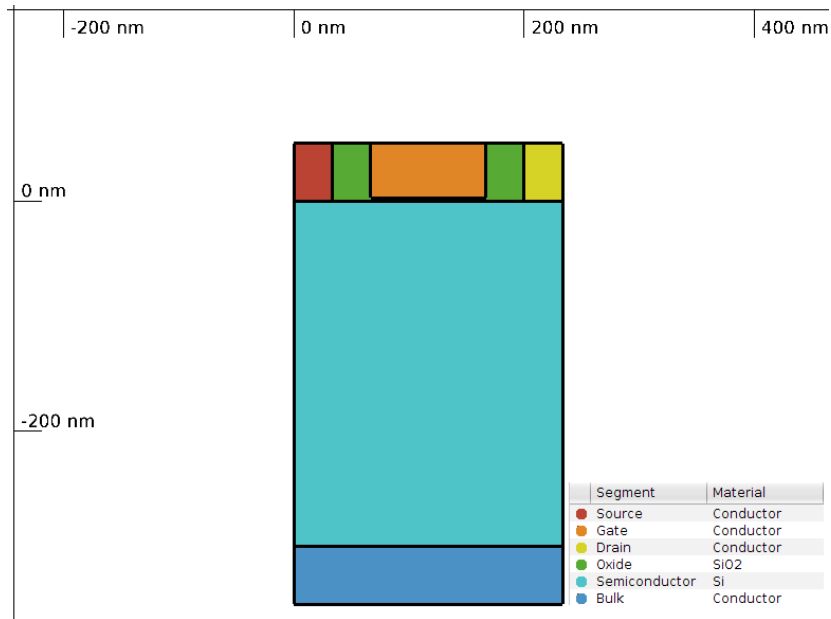


Fig. 18: Original 2D model of the considered pMOSFET device. The coloring (the same as in Fig. 14) illustrates the different materials which form the individual segments.

5.2.2 Automated RDD and NMP Simulations

In this thesis all simulations were performed using Minimos-NT. When simulating nanoscale devices quantum mechanical effects have to be considered. Quantum mechanical effects can be described by adding additional empirical terms, giving rise to the density gradient (DG) model. As mentioned in Section 3.2, the inclusion of discrete dopants requires the DG model. This is because the RDD model has been initially calibrated to nanoscale pMOSFETs using

the DG approach [2]. To select the DG iteration scheme for simulations the appropriate parameter has to be set in the corresponding `ipdm` file.

In Minimos-NT, two files are necessary to start a particular simulation: a structure file (`devbz`) and a simulation settings file (`ipdm`). The creation of them is described in the previous section. It has to be noted that the goal is to simulate 1,000 up to 5,000 different **randomly** created discrete dopant distributions (RDD simulations). Using Minimos-NT, a distinctive distribution is created by a deterministic (pseudo-) random number generator based on a **seed** (integer, value set by the user). Therefore, different seeds lead to different dopant distributions. The seed has to be set in the corresponding `ipdm` file.

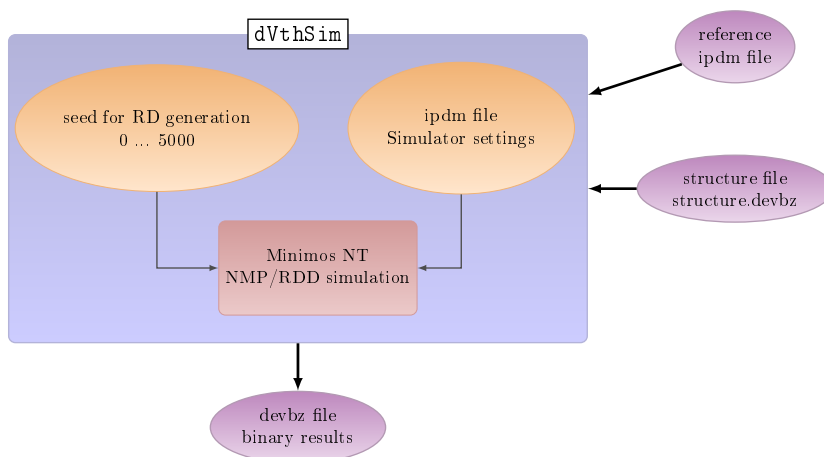


Fig. 19: Overview of the simulation procedure, part of work flow given in Fig. 16. The Python script `dVthSim` automated the simulation sequence involving Minimos-NT as central part.

The automated simulation process is realized by developing a Python script called `dVthSim`. Fig. 19 shows the conceptual work flow for **one** simulation corresponding to one seed. Actually, for every integer in the range from 0 to 5,000 (or 1,000) the reference `ipdm` file was altered by setting the seed to the according value. Together with the structure file (`structure.devbz`) it is passed to Minimos-NT to perform the simulation. In that way 5,001 (or 1,001) simulations are subsequently started and carried out. As gate voltage shift extraction requires a gate voltage sweep in order to obtain drain current and NMP transition time characteristics (see Fig. 6 and Fig. 10) every single simulation effectively consisted of 40 simulation steps. The seed value 0 turns RDD off and thus corresponds to a continuous dopant distribution [19]. The continuous simulation results are used as reference (see Section 5.2.4) to calculate the gate voltage shifts.

Apart from `ipdm` file creation, `dVthSim` manages the output folder structure and the memorization of the resulting output files (`devbz`). As mentioned above, every individual step during the gate voltage sweep produces one distinctive output file. It is important to point out, that the output `devbz` files contain the entire simulation results including potential, electron concentration, work function and much more. The extraction of the relevant parameters is the target of the next section.

5.2.3 Post-Processing

Minimos-NT provides a multitude of resulting physical quantities from the simulations. For the calculation of gate voltage shifts only gate voltage, drain current and capture/emission times are required. The output files, which contain those quantities, are saved in a binary file format. Unfortunately, no parser allowing direct extraction of the parameters has been

available and thus a workaround has to be employed.

Using the tool `gtsinfo` the binary devbz output file was converted to a **plain text deva** file. A **deva** file is simply a human-readable representation of the underlying data structure. Since MinimOS-NT uses an advanced cascaded pointer-to-pointer data management, parsing the resulting deva file is rather complicated. Supported by *Global TCAD Solutions* the Python script `parse_deva` has been successfully implemented.

The script `parse_deva` is capable of extracting any scalar parameters like '*potential*' from distinctive segments like '*bulk*'. In addition, the exact position of the acceptors and donors can be extracted. By being capable of these features, `parse_deva` actually provides more flexibility than essentially needed for gate voltage shift extraction. Thus, this script can be recommended for further investigations.

The so far discussed subtasks have been integrated in a Python script called `processDevice`. In Fig. 20 the procedure of post-processing work flow is illustrated. The script's main objective is to construct two output `crv` files for every seed (namely `nmp_trap_out.crv` and `minimos_out.crv`, see Fig. 20). The `crv` files contain the capture/emission times or the drain current as a function of gate voltage, respectively.

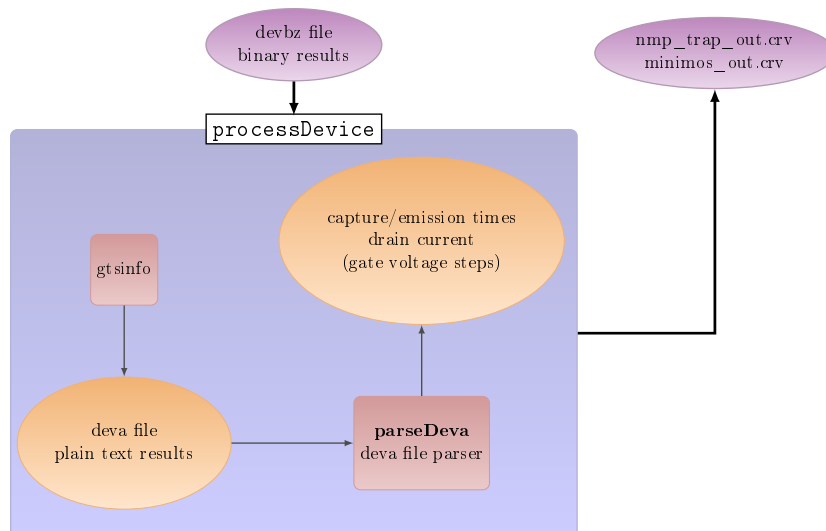


Fig. 20: Illustration of the post processing procedure, part of work flow given in Fig. 16. It is implemented by the Python script `processDevice`.

5.2.4 ΔV_g Extraction

After the processing described in the previous section the produced `crv` files have to be statistically evaluated. As can be seen in Fig. 21 a lateral shift of the $I_d(V_g)$ and the $\tau_{c,e}(V_g)$ characteristics is obtained when RDD are considered during our simulations. The assumption that RDD causes a lateral shift of the reference characteristics, however, is only true in a defined finite interval. Especially the capture time characteristics deviate from the reference's shape for $V_g < -1$ V. It is important to note that the capture and emission times can only be reasonably analyzed inside those intervals, where experimental data points are available (see Fig. 6). A further detailed knowledge of $\tau_{c,e}(V_g)$ characteristics would require more experimental investigations. Therefore, for the application of the *lateral shift method* it is sufficient that the prerequisite of Section 4.2 is fulfilled inside the interval -3 V $< V_g < -1$ V for capture times and -1 V $< V_g < 1$ V for emission times. Fig. 21 show that this is the case, thus the *lateral shift method* can be applied.

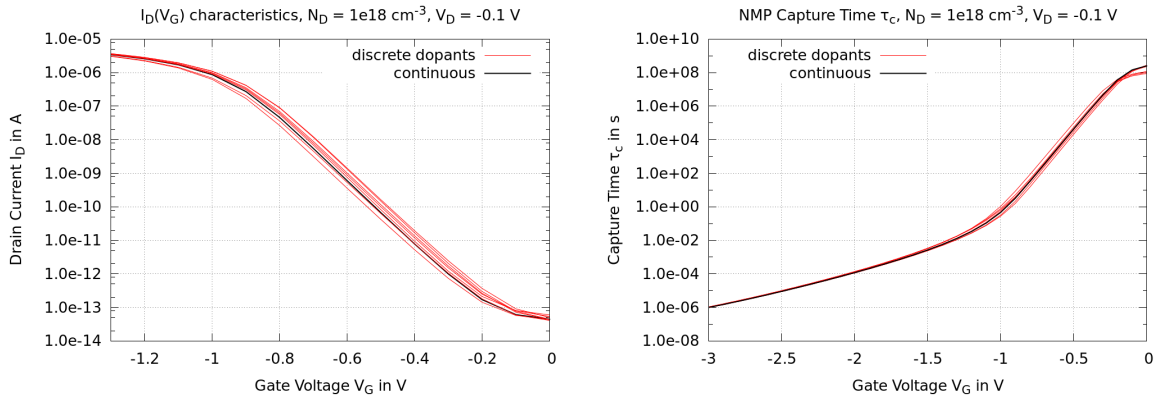


Fig. 21: Left: Using different random discrete dopant distributions produces a set of $I_d(V_g)$ curves (red) which are shifted relative to the one originating from assuming a continuous doping distribution (black). **Right:** The gate voltage dependence of the capture times shows different lateral shifts for different RDD distributions.

The *lateral shift method* is implemented by two Python scripts called `deltaVgExtractionNMP`, `deltaVgExtractionId`, which allowed automated extraction and both are summarized in Fig. 22 as `deltaVgExtraction`.

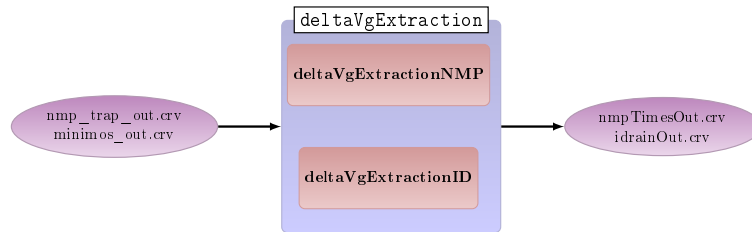


Fig. 22: The ΔV_g extraction procedure is part of work flow given in Fig. 16. The Python scripts `deltaVgExtractionNMP` and `deltaVgExtractionId` implement the *lateral shift method* described in detail in Section 4.2.

The extraction scripts strictly implement the *lateral shift method*. Thus, polynomial fits (on logarithmic scale), the cost function and the golden section search are included. The minimum of the cost function is searched by **two golden section search iterations** (one with halved starting interval) and another additional call of `scipy`'s [23] function `fmin`. The Python implementation of `fmin` uses the Nelder-Mead method and needs an initial guess, which is chosen close to zero [24]. By evaluating the cost function at the three obtained minima, the best gate voltage shift is found. Three different search runs are carried out to minimize the possibility of falsely yielding a local minimum. Extracts from `deltaVgExtractionNMP` are given below.

Listing (deltaVgExtractionNMP)

```
def interpolated_log(vg, tauc, fitInterval, order):
    xv = [ ], yv = [ ]
    for i, v in enumerate(vg):
        if v >= fitInterval[0] and v <= fitInterval[1]:
            xv += [ v ]
            yv += [ log10(tauc[i]) ]
```

```

#return coefficients of polynomial: a_n, ... a_2, a_1, a_0
return polyfit(xv, yv, order)

def polynomial(x, coeff):
    poly_value = 0
    deg        = poly_degree(coeff)

    for i, c in enumerate(coeff):
        poly_value += coeff[deg - i - 1] * x**i

    return poly_value

#score function = cost function
def scorefunction(deltaVg, coeffSim, coeffRef, fitInterval):
    STEP_N     = 250
    error      = 0
    x          = linspace(fitInterval[0], fitInterval[1],
                          num=STEP_N).tolist()

    for i in x:
        error += (polynomial(i, coeffRef) -
                  polynomial(i - deltaVg, coeffSim))**2

    return error

def calculateVgShift(referencePath, simPath):
    .
    .
    .

#fit polynomial to log tauc inside measurement data interval
fitInterval = (-2.4, -1)
coeffRef    = interpolated_log(vgR, taucRef, fitInterval, 4)
coeffSim    = interpolated_log(vgR, taucSim, fitInterval, 4)

#find minimum
#gss ... golden section search
deltaVg_g   = gss(scorefunction, -2, 2,
                  fargs = (coeffSim, coeffRef, fitInterval))
deltaVg_l   = gss(scorefunction, -1, 1,
                  fargs = (coeffSim, coeffRef, fitInterval))

initialGuess = 0.1
deltaVg_n    = fmin(scorefunction, initialGuess,
                   args = (coeffSim, coeffRef, fitInterval))[0]

f_g = scorefunction(deltaVg_g, coeffSim, coeffRef, fitInterval)
f_n = scorefunction(deltaVg_n, coeffSim, coeffRef, fitInterval)
f_l = scorefunction(deltaVg_l, coeffSim, coeffRef, fitInterval)

```

As illustrated in Fig. 22, the extraction process produces output `crv` files, which contain the seed value and the corresponding ΔV_g value. The subsequent statistical analysis is described in the next section.

5.2.5 Statistical Analysis and Visualization

For the purpose of statistical analysis the Python script `batchHistogram` (see Fig. 23) is implemented. It is capable of

- extracting the statistical parameters (mean, standard deviation, skew(ness)),

- generating histograms and
- plotting the empirical cumulative distribution function (eCDF).

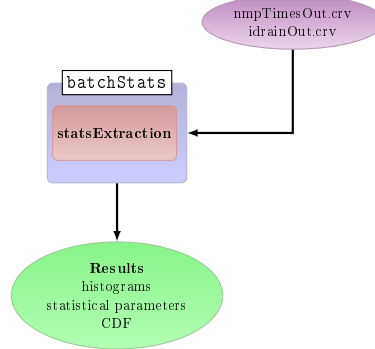


Fig. 23: ΔV_g statistical analysis as part of the work flow given in Fig. 16. The Python script `batchStats` calculates statistical parameters and creates histograms and eCDFs by using `gnuplot`.

The statistical parameters are extracted directly from the (output) crv files `nmpTrapOut.crv` or `idrainsOut.crv` using the **sample mean**

$$\overline{\Delta V_g} = \frac{1}{N} \sum_{i=1}^N \Delta V_{g,i}, \quad (6)$$

the sample standard deviation

$$s(\Delta V_g) = \sqrt{\frac{1}{N-1} \sum_{i=1}^N (\Delta V_{g,i} - \overline{\Delta V_g})^2} \quad (7)$$

and the sample skewness [25]

$$g(\Delta V_g) = \frac{\sqrt{(N-1)N}}{N-2} \frac{\frac{1}{N} \sum_{i=1}^N (\Delta V_{g,i} - \overline{\Delta V_g})^3}{\left(\frac{1}{N} \sum_{i=1}^N (\Delta V_{g,i} - \overline{\Delta V_g})^2\right)^{3/2}}, \quad (8)$$

where N is the number of simulations with different discrete dopant distributions.

The histograms are plotted using `gnuplot`. It has to be noted that histograms generally are significant only if the width of the bins is suitably chosen. Since a-priori estimation of the appropriate bin width is difficult in automated histogram generation, additionally the empirical cumulative distribution function (eCDF) is plotted. The eCDF is defined as [26]

$$\hat{F}(\Delta V_g) = \frac{1}{N} \sum_{i=1}^N I_{(-\infty, \Delta V_g]}(\Delta V_{g,i}), \quad (9)$$

where I denotes the *indicator function*, given by

$$I_A(x) := \begin{cases} 1 & \text{if } x \in A, \\ 0 & \text{if } x \notin A. \end{cases} \quad (10)$$

When using eCDFs no a-priori choices have to be made. However, cumulative distribution functions are not always easy to interpret. A possible auxiliary tool is the probit function, which is further discussed in Chapter 6.

6 Results

The simulation and post-processing work flow described in Chapter 5 shows the entire process flow used to get information on how RDD influence macroscopic $I_d(V_g)$ and microscopic $\tau_{c,e}(V_g)$ characteristics of single traps. In Section 2 it is presented that the study of NBTI is a major issue regarding device reliability. Fig. 14 shows the model for an actual pMOSFET which has been experimentally investigated using TDDS (see Section 2.3). The experiments resulted in capture and emission time versus gate voltage characteristics $\tau_{c,e}(V_g)$ as depicted in Fig. 6. It is important to note that the acquired emission times τ_e of a single trap showed no gate voltage dependence, a behavior we link to so called fixed traps. Based on the experimental results the four-state NMP model has been calibrated to reproduce the experimental time characteristics. The final configuration of the four-state NMP model's parameters is presented in Appendix A.

With the four-state NMP model being calibrated, the $\tau_{c,e}(V_g)$ and additionally $I_d(V_g)$ characteristics in presence of discrete dopants can be simulated and analyzed using the procedure presented in Section 5.2.4. In the following the impact of channel doping and trap position on the ΔV_g distribution is presented and discussed. It has to be noted that ΔV_g distributions are equivalent to threshold voltage shift (ΔV_{th}) distributions.

6.1 Normal Trap at Fixed Position

In Chapter 5 the investigated pMOSFET structure is presented (Fig. 14). Since the impact of RDD distributions is determined by the prevalent acceptor or donor concentration, a strong doping dependence of ΔV_g distributions is expected. For the discussed pMOSFET the continuous acceptor and donor distribution model is appropriately chosen to obtain the same global operational properties as the investigated structure has shown in experiment. The resulting distributions are shown in Fig. 24. In a pMOSFETs, the channel interaction with the oxide is defined by donor concentration, which has in the underlying case a peak value of 10^{18} cm^{-3} . The doping distribution given in Fig. 24 is therefore called '10¹⁸ cm⁻³-doping' in the following.

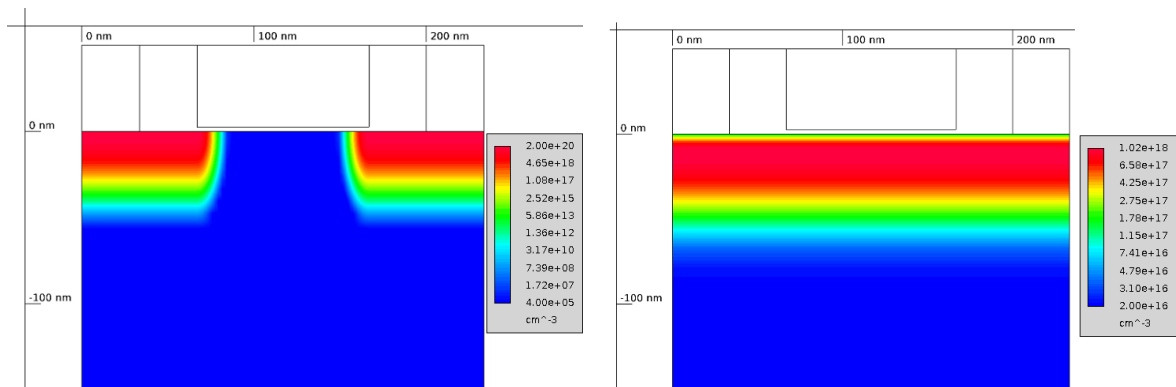


Fig. 24: Left: Acceptor concentration and Right: donor concentration for the considered pMOSFET.

To characterize the basic RDD distribution influence on the capture and emission times, the simple case of a **single trap** is considered first. Two different simulation settings are set up. One with a single trap located at the **center point of the channel** and another one with the defect near the **source contact**.

6.1.1 Single Fixed Trap located at Center of Gate Oxide

For the first investigations, a single defect is placed at the geometric center of gate oxide region, as illustrated in Fig. 25). It is has to be noted that this particular and all further traps are positioned 0.354 nm above semiconductor-oxide interface. This position is given by the four-state NMP model and is a crucial parameter when simulated capture and emission times are adjusted to experimental data. The doping concentration is set to the distribution depicted in Fig. 24.

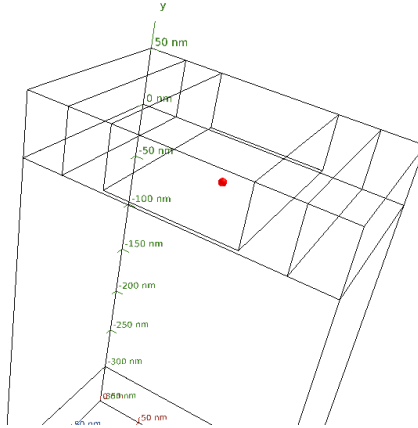


Fig. 25: Illustration of the 3D model of the used structure. The red sphere indicates the position of the single trap. Along the y-axis the trap is located at distance of 0.354 nm away from semiconductor-oxide interface towards the gate, which is a result of the four-state NMP model.

For gate voltage shift extraction 5,000 different discrete dopant distributions have been simulated and processed with the methods described in Chapter 5. The resulting histograms can be seen in Fig. 26. The ΔV_g values obtained from the $I_d(V_g)$ characteristics are found to be **normally distributed** (Fig. 26b). As expected based on the fact that the individual discrete dopant distributions are derived from continuous distributions, the mean value is close to zero.

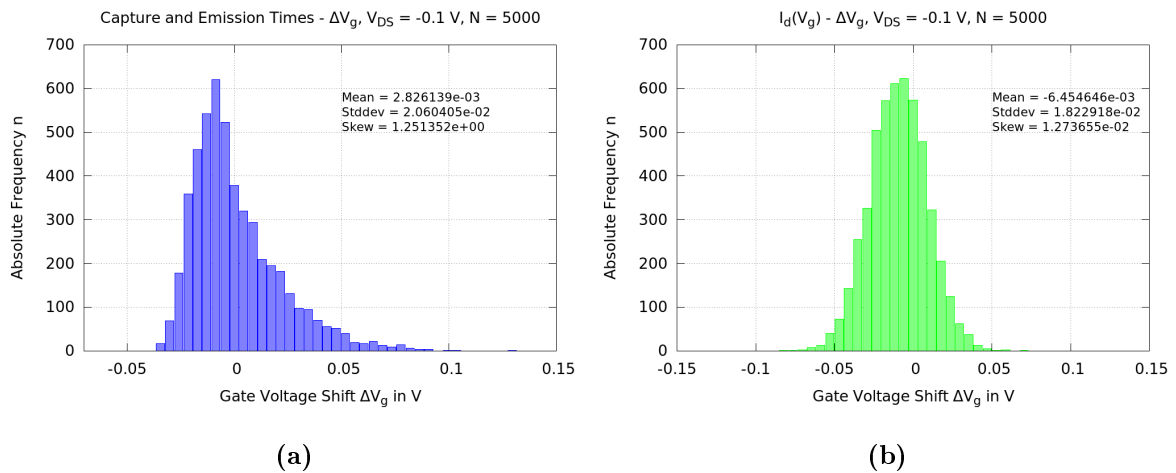


Fig. 26: Gate voltage shift histograms for a single fixed trap located at the center point of gate oxide and for a donor concentration of 10^{18} cm^{-3} . **a)** ΔV_g extracted from $\tau_{c,e}(V_g)$ characteristics, **b)** ΔV_g obtained from transfer characteristics. The drain-source voltage V_{DS} is set to constant -0.1 V .

The gate voltage shifts obtained from $\tau_{c,e}(V_g)$ characteristics, do not show a normal distribution, but are possibly **Weibull** distributed, see Fig. 26a. To eliminate possible misinterpreta-

tions arising from the binning of the histogram, empirical cumulative distribution functions (eCDFs) (9) are calculated and plotted in Fig. 27. eCDFs provide a further analysis method, which is based on *quantile* or *inverse cumulative distribution functions*. To test if an underlying data set is normally distributed, the inverse cumulative distribution function of the standard normal distribution (which is called *probit* function)

$$P(p) = \sqrt{2} \operatorname{erf}^{-1}(2p - 1) \quad (11)$$

is calculated. If the tested distribution is normally distributed $X \sim \mathcal{N}(\mu, \sigma^2)$ with Mean μ and variance σ^2 the cumulative distribution function is given by

$$\Phi(x) = \frac{1}{2} \left[1 + \operatorname{erf} \left(\frac{x - \mu}{\sigma\sqrt{2}} \right) \right]. \quad (12)$$

The function composition $(P \circ \Phi)(x) = P(\Phi(x))$ yields

$$\Phi(x) = \sqrt{2} \operatorname{erf}^{-1} \left[1 - 1 + \operatorname{erf} \left(\frac{x - \mu}{\sigma\sqrt{2}} \right) \right] = \frac{x - \mu}{\sigma}, \quad (13)$$

which is a linear function. In Fig. 28 the probit function was plotted for the eCDFs from Fig. 27. The ΔV_g values obtained from $I_d(V_g)$ characteristics clearly transforms to a linear function, confirming a normally distributed data set. In contrast, the eCDFs originating from $\tau_{c,e}(V_g)$ characteristics do not transform to a linear function. Thus, the gate voltage shifts obtained from the $\tau_{c,e}(V_g)$ characteristics can not be described by a simple normal distribution.

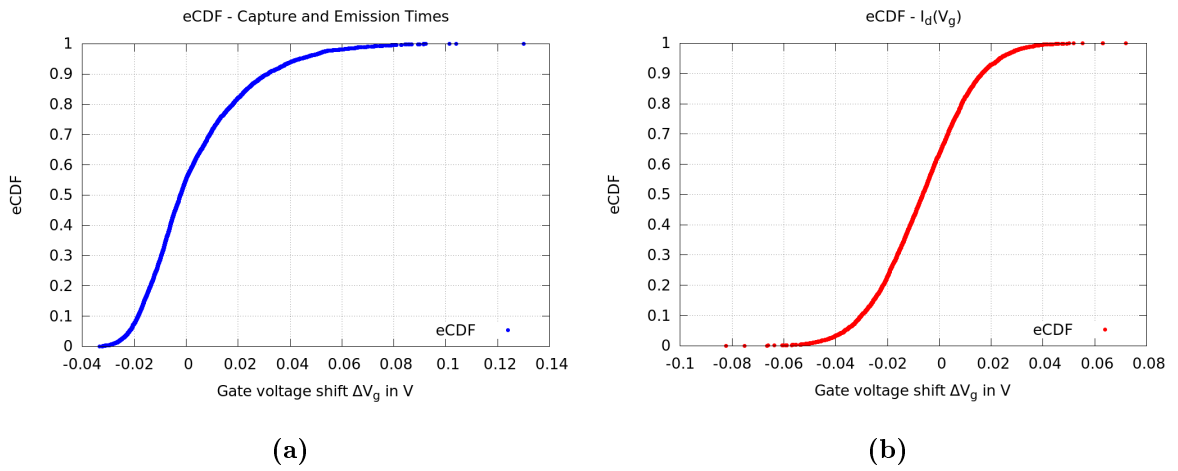


Fig. 27: The empirical cumulative distribution functions (eCDFs, eqn. 9) for a single fixed trap located at the center of the gate oxide and a donor concentration of 10^{18} cm^{-3} . **a)** ΔV_g extracted from $\tau_{c,e}(V_g)$ characteristics and **b)** ΔV_g obtained from transfer characteristics.

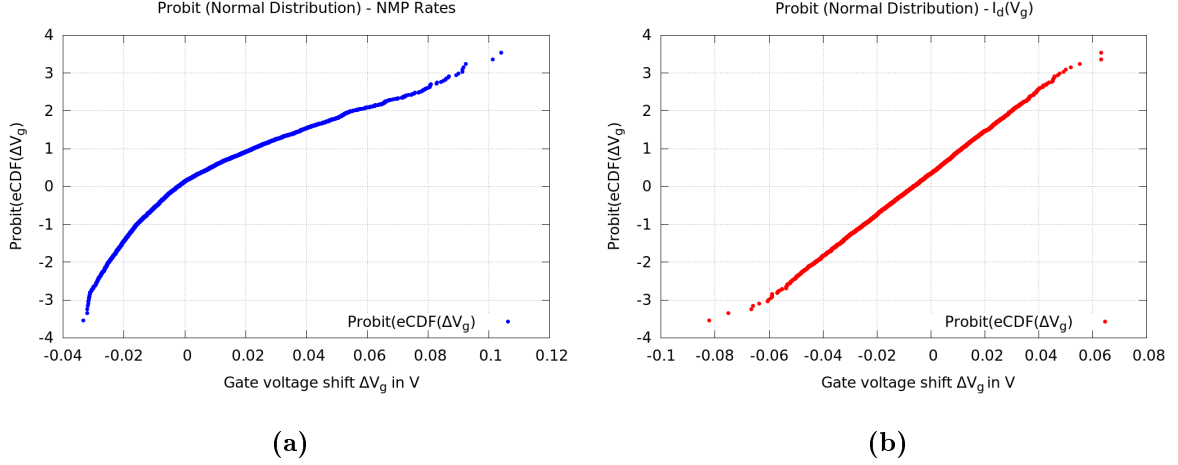


Fig. 28: The probit functions (eqn. 11) applied on the empirical cumulative distribution functions (eCDFs) for a single fixed trap located at the center of the gate oxide and a donor concentration of 10^{18} cm^{-3} . **a)** ΔV_g extracted from $\tau_{c,e}(V_g)$ characteristics, **b)** ΔV_g obtained from transfer characteristics. As b) represents nearly a perfect straight line, this distribution can be considered normally distributed. In contrast, the distribution from a) cannot be described by a normal distribution.

For the next simulations the bulk doping concentration is altered. More precisely, the donor concentration is pointwise reduced or raised by the **factor of 10**. The resulting histograms are compared in Fig. 29. The ΔV_g values extracted from the calculated capture and emission time are very noticeable. Fig. 29a clearly shows an elevated doping concentration dependence. For donor concentration $N_D = 10^{17} \text{ cm}^{-3}$ the ΔV_g distribution shows a sharp peak located around $\Delta V_g = 0 \text{ V}$. This means that the impact of RDD on capture and emission times is **negligible**. An increased donor concentration ($N_D = 10^{19} \text{ cm}^{-3}$) leads to significant **broadening** of the ΔV_g distribution. Furthermore, the gate voltage shifts for this doping concentration can be considered **normally** distributed.

The ΔV_g distribution based on transfer characteristics maintains the normal distributed shape and show a **broadening** with rising donor concentration (Fig. 29b). Most surprisingly, a **mean value shift** towards negative values, is clearly observable. The statistical parameters for the distributions shown in Fig. 29 are summarized in Tab. 1 and Tab. 2.

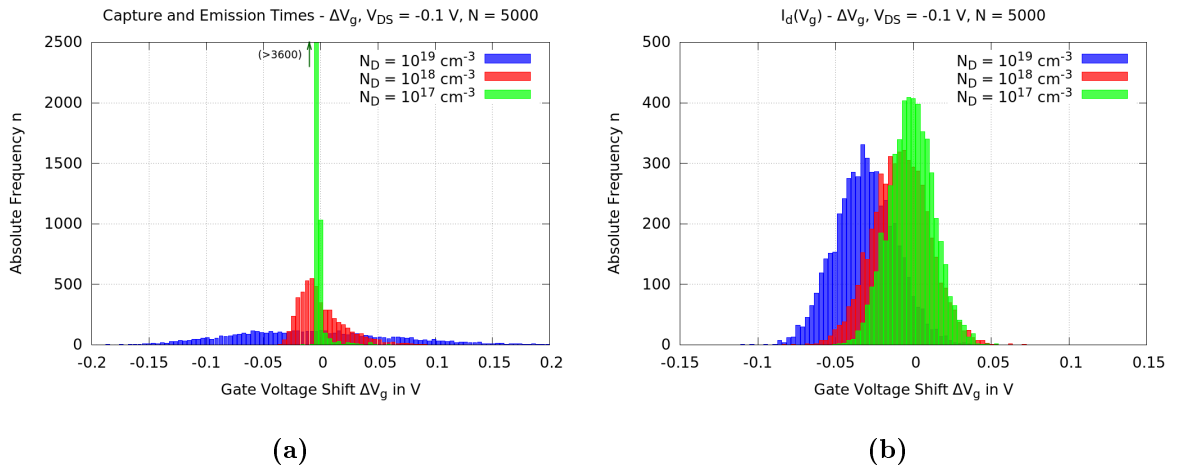


Fig. 29: Gate voltage shift histograms for a single fixed trap located at the center of the gate oxide for different donor concentrations. **a)** ΔV_g extracted from $\tau_{c,e}(V_g)$ characteristics and **b)** ΔV_g obtained from transfer characteristics.

N_D in cm^{-3}	μ in V	σ in V	g
10^{17}	1.65e-04	5.25e-03	6.33
10^{18}	2.83e-03	2.06e-02	1.25
10^{19}	-5.21e-03	7.05e-02	0.35

Tab. 1: Statistical parameters mean μ , standard deviation σ and skewness g for different donor concentration N_D . The gate voltage shift distributions were obtained from the $\tau_{c,e}(V_g)$ characteristics and the corresponding histograms are given in Fig. 29a.

N_D in cm^{-3}	μ in V	σ in V	g
10^{17}	3.79e-04	1.43e-02	3.25e-02
10^{18}	-6.45e-03	1.82e-02	1.27e-02
10^{19}	-2.93e-02	1.96e-02	8.26e-02

Tab. 2: Statistical parameters mean μ , standard deviation σ and skewness g for different donor concentration N_D . The gate voltage shift distributions were obtained from the $I_d(V_g)$ characteristics and the corresponding histograms are shown in Fig. 29b.

6.1.2 Single Fixed Trap near the Source Side of the Channel

Next we want to account for the dependence of the ΔV_g distribution on the trap position. Therefore, the trap is placed near the source side of the channel, highlighted by the green square in Fig. 30. For the sake of completeness, the central trap position considered in Section 6.1.1 is marked with a violet square.

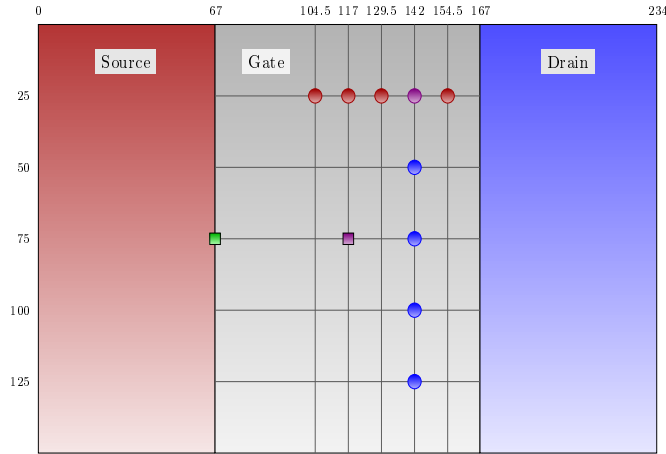


Fig. 30: Schematic top view of the different trap position investigated for the pMOSFET. The violet square illustrates the trap located at the center point as discussed in Section 6.1.1, the green square indicates the trap located at the source side of the channel (Section 6.1.2). The circles denote the positions investigated in Section 6.2, red: Fig. 34, blue: Fig. 35. The violet circle indicates that this position is included in both (Fig. 34 and Fig. 35). All dimensions are given in nm.

For the trap located at the source side of the channel 5,000 simulations are carried out and the resulting histograms for a donor concentration of $N_D = 10^{18} \text{ cm}^{-3}$ are shown in Fig. 31. Whereas the transfer characteristics show the same ΔV_g distributions obtained from the trap located in the center of the device, a different and noteworthy ΔV_g distribution for the capture and emission times is visible, see Fig. 31. Apart from the dominating peak around zero, an additional **small side peak** can be observed.

Varying the donor concentration leads to the histograms shown in Fig. 32. By comparing Fig. 32b and Fig. 29b it is visible that a change of trap position **does not alter** the ΔV_g distributions associated with $I_d(V_g)$ characteristics. The ΔV_g distributions obtained from $\tau_{c,e}(V_g)$ characteristics, see Fig. 32a, **remain unchanged** for the considered donor concentrations. The statistical quantities listed in Tab. 3 support this findings. It is imported to note that the acceptor doping which predominantly affects source region **has not been altered**. Based on the observation that the ΔV_g distribution does not change with varying donor concentration we conclude that the statistical variation of the donor atoms is negligible. However, the capture and emission times are seriously determined by the electrostatic potential present within the channel. For the trap located at the source side electrostatics is dominated by the high acceptor concentration of the source region.

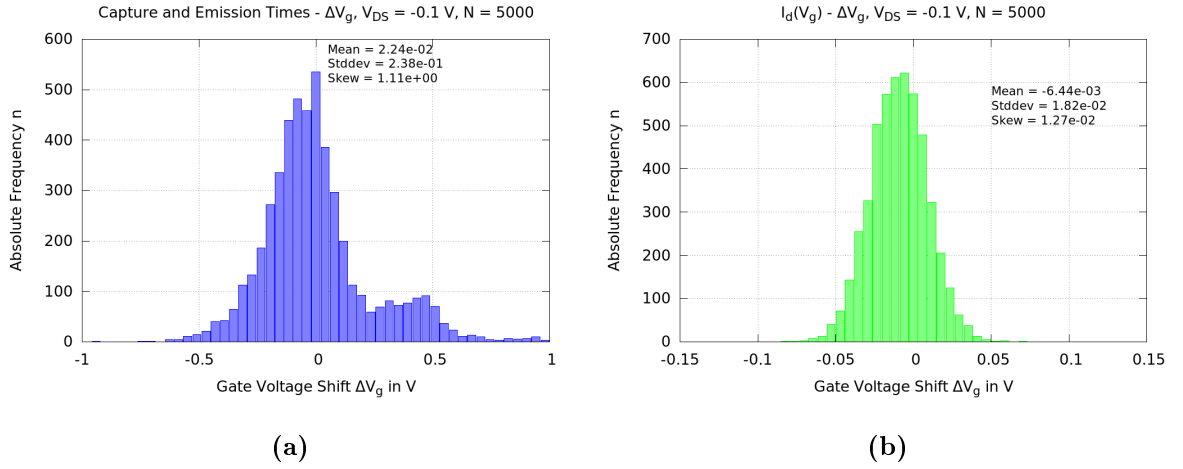


Fig. 31: Gate voltage shift histograms for a single fixed trap located near the source side of the channel for the pMOSFET with a donor concentration of 10^{18} cm^{-3} . **a)** ΔV_g extracted from $\tau_{c,e}(V_g)$ characteristics and **b)** ΔV_g obtained from transfer characteristics.

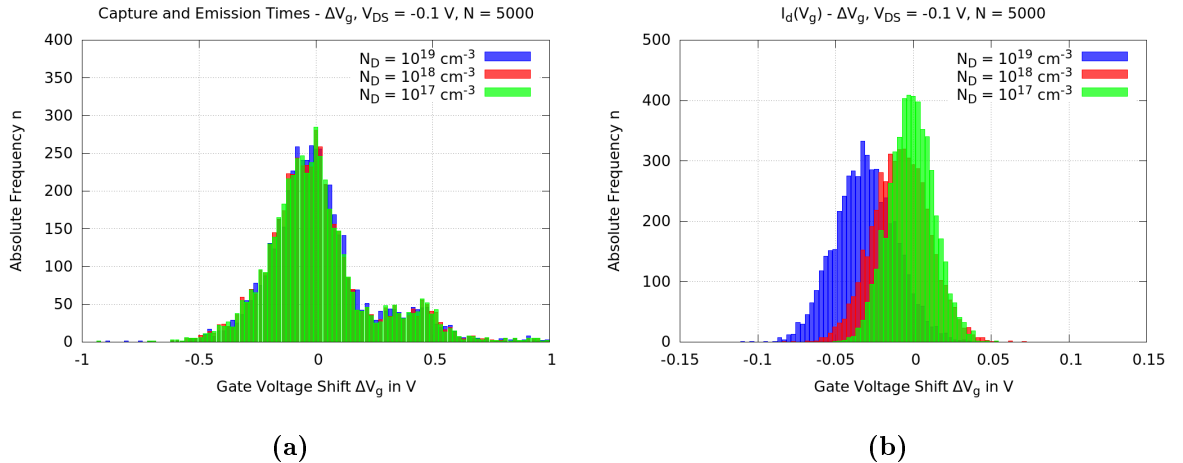


Fig. 32: Gate voltage shift histograms for the pMOSFET with a single fixed trap located near the source side of the channel and **varying** donor concentrations. **a)** ΔV_g extracted from $\tau_{c,e}(V_g)$ characteristics and **b)** ΔV_g obtained from transfer characteristics.

N_D in cm^{-3}	μ in V	σ in V	Skewness g
10^{17}	2.19e-02	2.38e-01	1.11
10^{18}	2.24e-02	2.38e-01	1.11
10^{19}	3.00e-02	2.31e-01	1.15

Tab. 3: Statistical parameters mean μ , standard deviation σ and skewness g for different donor concentration N_D . The gate voltage shift distributions were obtained from the $\tau_{c,e}(V_g)$ characteristics and the corresponding histograms are visible in Fig. 32a.

So far the ΔV_g distributions extracted from $I_d(V_g)$ and $\tau_{c,e}(V_g)$ characteristics have been analyzed separately. In order to check for a possible **statistical correlation** between both distributions, correlation plots are created and shown in Fig. 33. As can be seen, a weak correlation is visible for the data from the trap located at the center point of the pMOSFET's channel. To quantify a possible *linear* correlation the correlation coefficient

$$r = \frac{\sum_{i=1}^n (x_i - \bar{x})(y_i - \bar{y})}{\sqrt{\sum_{i=1}^n (x_i - \bar{x})^2} \sqrt{\sum_{i=1}^n (y_i - \bar{y})^2}} \quad (14)$$

is evaluated. The correlation coefficient for the trap located in the center is $r = 0.337$ and for the trap located near the source side $r = -0.004$. In the first case only a weak *linear* correlation is thereby present, whereas in the second case no *linear* correlation is prevalent. It is important to note that a non-linear correlation can not be excluded, as it would require further investigations [26].

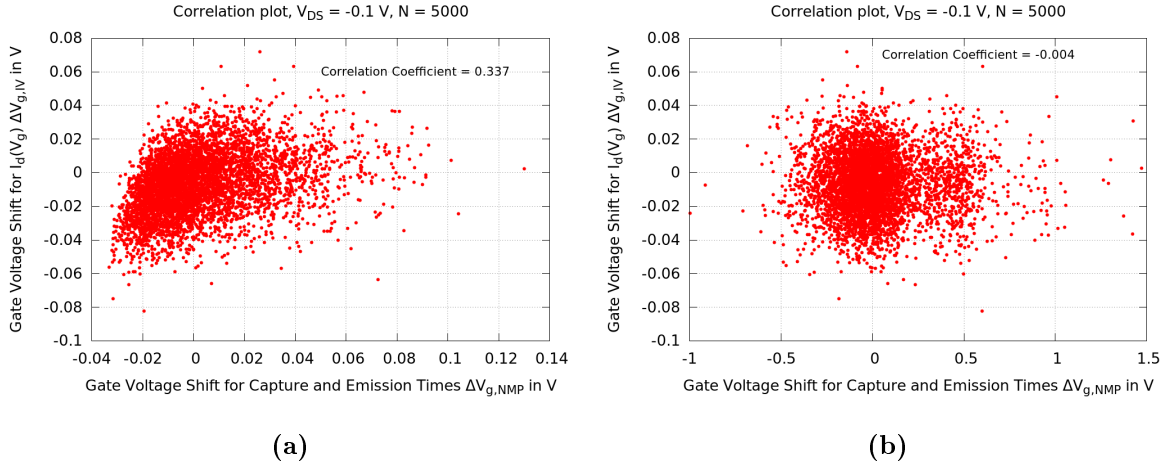


Fig. 33: Correlation diagrams for one single fixed trap located **a)** at the center point of gate oxide and **b)** near the source side of the channel. The donor concentration is for both cases set to $N_D = 10^{18} \text{cm}^{-3}$.

6.2 Influence of Trap Position

The observed strong position dependence of ΔV_g distributions suggest further investigations. For that 25 additional trap positions are simulated. In Fig. 30 the different investigated trap positions are indicated by the intersection of the gray lines inside gate region. The donor concentration is set to constant $N_D = 10^{18} \text{cm}^{-3}$ and for each trap position 1,000 simulations are carried out. The subsequent simulation data analysis is based on the same techniques described in the previous sections. A characteristic behavior when altering the position horizontally (between source and gate) and vertically can be observed.

The positions that are marked with red circles in Fig. 30 (including the violet circle) are considered first to study the **horizontal trap position dependence** on the ΔV_g distributions.

The corresponding histograms can be seen in Fig. 34. For the ΔV_g distributions based on $\tau_{c,e}(V_g)$ characteristics essentially a Weibull distribution is observable for all positions. The closer the trap is located to the drain side of the channel, the narrower and more pronounced is the peak. The ΔV_g values obtained from transfer characteristics, however, do not change along horizontal variation.

The investigations of the **vertical trap position dependence** are shown in Fig. 35, where it can be seen that the histograms only change slightly. These results suggest that on one hand the transfer characteristics remain unaffected by position variation, while on the other hand the distance between source/drain regions and trap position hugely affects $\tau_{c,e}(V_g)$ characteristics.

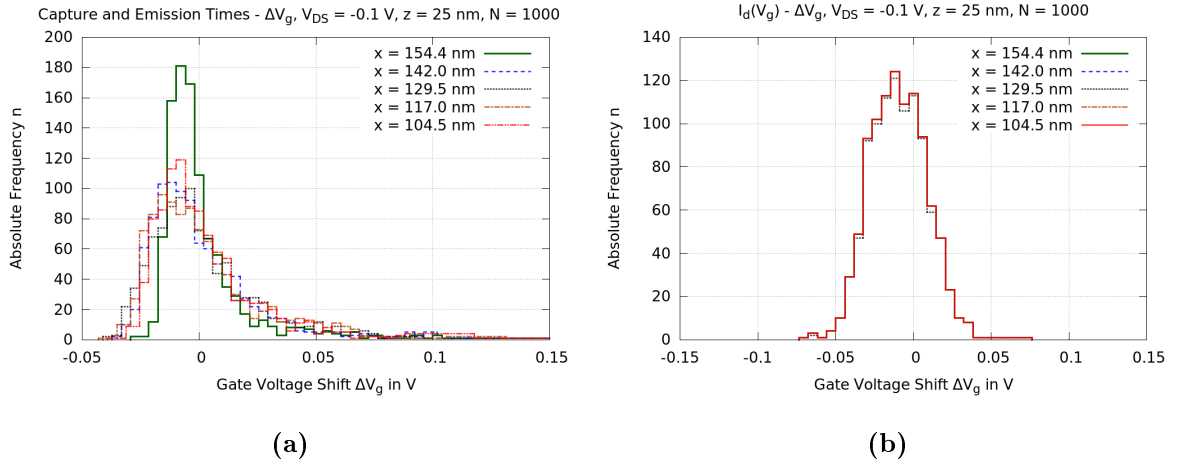


Fig. 34: ΔV_g distributions for different trap positions which are visible as red circles in Fig. 30. The **horizontal variation** of the trap position has an impact on the ΔV_g distribution calculated from **a)** $\tau_{c,e}(V_g)$ characteristics. In contrast the **b)** $I_d(V_g)$ characteristics appear unaffected by the varying trap position. The donor concentration is set to $N_D = 10^{18}$ cm $^{-3}$.

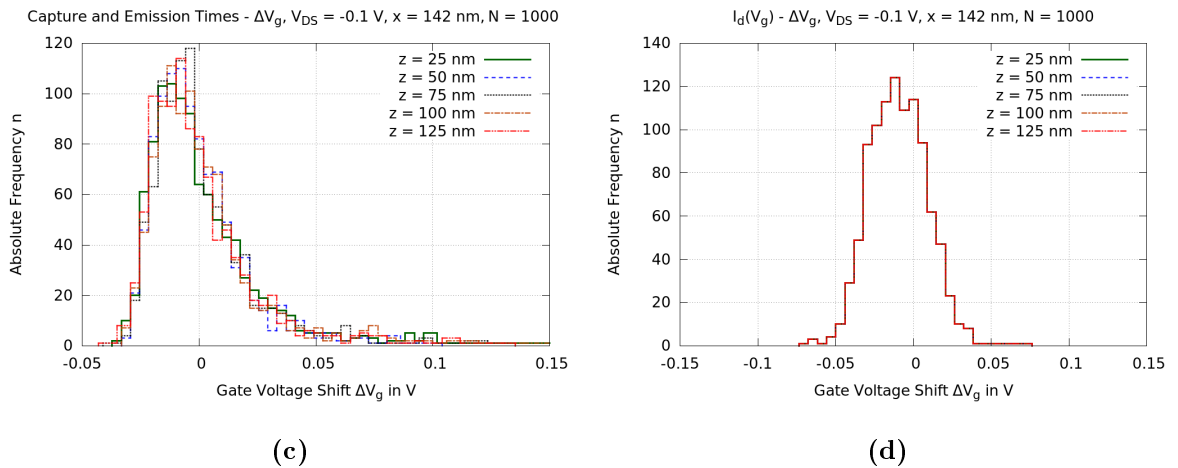


Fig. 35: ΔV_g distributions for different trap positions which are visible as red circles in Fig. 30. The **vertical variation** of the trap position has only a negligible impact on both the ΔV_g distribution calculated from **a)** $\tau_{c,e}(V_g)$ characteristics and **b)** $I_d(V_g)$ characteristics. The donor concentration is set to $N_D = 10^{18}$ cm $^{-3}$.

7 Summary and Outlook

In this thesis the interaction between two individually developed and implemented models, namely the four-state NMP model and the random discrete dopants (RDD) approach, was investigated. Both models are implemented in the established general purpose semiconductor device simulator Minimos-NT developed at the Institute for Microelectronics. A data processing algorithm called *lateral shift method* enabled a quantification of that interaction by calculating gate voltage shifts ΔV_g , which are equivalent to the threshold voltage shifts ΔV_{th} . The following results were obtained from analyzing a pMOSFET structure with geometrical dimensions of width \times length = 150 nm \times 100 nm and one single fixed trap placed inside the gate oxide:

- Gate voltage shifts ΔV_g obtained from the macroscopic **transfer** characteristics are **normally distributed**. Mean value and standard deviation are independent from trap position and donor concentration. In particular, varying trap positions do **not** cause a change of those statistical parameters.
An **increase** of the donor concentration causes a shift of the mean value of ΔV_g towards **more negative values**.
- Gate voltage shifts derived from the microscopic **capture and emission time** characteristics (calculated by employing the initially calibrated four-state NMP model) are very sensitive to both, trap position and donor concentration. For the former, the distance between the trap position and source or drain region is essential. If the trap is located **close** to the source/drain side of the channel, the capture and emission times **do not depend on donor concentration**, but are determined by acceptor concentration, which predominantly define electrostatics there.
For a trap placed at the center of the gate oxide variation of donor concentration leads to a **alteration** of the underlying probability distribution (listed in Tab. 4).
- In the case of traps located near source or drain, the resulting ΔV_g distributions extracted from capture/emission time characteristics surprisingly show a second peak (Fig. 31a).
- The analysis if any correlation between ΔV_g distributions obtained from transfer characteristics and ΔV_g distributions from capture and emission time characteristics is present reveals a **weak linear correlation** for traps located at the **center** traps and **no linear correlation** for traps located **near the source side** of the channel.

Donor Concentration N_D in cm^{-3}	Probability Distribution
10^{17}	Delta Distribution located at $\Delta V_g = 0$
10^{18}	Weibull
10^{19}	Gaussian

Tab. 4: Summary of ΔV_g probability distributions obtained from $\tau_{c,e}(V_g)$ characteristics for different donor concentrations. The corresponding histograms are shown in Fig. 29a

In an extensive study the impact of RDD on the capture and emission times calculated using the four-state NMP model was investigated. To strengthen the findings in this work a larger number of traps with different four-state NMP model parameter sets relying on experimental data of different defects have to be analyzed. The origins of the prevalent second peak in the gate voltage shift distributions for traps located near source or drain have to be further investigated. Additionally, different MOSFET technologies, for instance high-k gate oxide structures, have to be studied. As noted within this work, RDD weakly influence

the capture and emission time characteristics. This would lead to slightly different four-state NMP model parameters for different dopant distributions, a circumstance not considered so far. Furthermore, a more refined trap position variation analysis is also required. Finally, based on further investigations a more complex understanding of the trapping kinetics and interplay between device physics and device reliability can be achieved.


```

        captureCrossSection      = 1.392604400379e-14 "m^2";
        captureCrossSection_metal = 1.61137127020717e-18 "m^2";
        attemptFrequency         = 10000000000000.0 "1/s";
        trapType                  = "Hole";

        R12p_mean      = 0.553921262571387;
        S12p_mean      = 1.30836092232229;
        R1p2_mean      = 1.0;
        S1p2_mean      = 50.0;
        EpsT2_mean     = 0.430469829727224 "eV";
        Eps1p1_mean    = 0.4 "eV";
        Eps2p2_mean    = 0.424122660327096 "eV"; // 0.5 //0.3 "eV";

        bandEdgeApproximation = false;
        tunnelingSegments     = "Gate, Semiconductor";
    }
}
}
}
+Source = 0.0 "V";
+Gate   = step(1 "V", -3 "V", 0.10 "V") ;
+Drain  = -0.1 "V";
+Bulk   = 0.0 "V";
}
Iterate : IterateDefaults
{
    Scheme : SchemeDefaults.DG
    {
    }
}
Curve : CurveDefaults
{
    Response
    {
        +VSource = output("Device", "V", "Source");
        +ISource = output("Device", "I", "Source");
        +VGate   = output("Device", "V", "Gate");
        +IGate   = output("Device", "I", "Gate");
        +VDrain  = output("Device", "V", "Drain");
        +IDrain  = output("Device", "I", "Drain");
        +VBulk   = output("Device", "V", "Bulk");
        +IBulk   = output("Device", "I", "Bulk");
    }
}
.
.
.

Solve : SolveDefaults
{
T = 398 K;
}

```


References

- [1] T. Grasser, “Stochastic Charge Trapping in Oxides: From Random Telegraph Noise to Bias Temperature Instabilities,” *Microelectronics Reliability*, vol. 52, no. 1, pp. 39–70, 2012.
- [2] B. Schwarz, “Simulation of Random Dopant Fluctuations with a Quantum-Corrected Drift-Diffusion Model,” *Master’s Thesis, TU Wien*, 2011.
- [3] R. Entner, *Modeling and Simulation of Negative Bias Temperature Instability*, Ph.D. thesis, TU Wien, 2007.
- [4] D. Schroder, “Negative Bias Temperature Instability: What do we Understand?,” *Microelectronics Reliability*, vol. 47, no. 6, pp. 841–852, 2007.
- [5] B. Kaczer, T. Grasser, J. Franco, M. Toledano-Luque, Ph. J. Roussel, M. Cho, E. Simoen, and G. Groeseneken, “Recent Trends in Bias Temperature Instability,” *Journal of Vacuum Science & Technology B*, vol. 29, no. 1, 2011.
- [6] V. Huard, M. Denais, and C. Parthasarathy, “NBTI Degradation: From Physical Mechanisms to Modelling,” *Microelectronics Reliability*, vol. 46, no. 1, pp. 1–23, 2006.
- [7] B. G. Streetman and S. K. Banerjee, *Solid State Electronic Devices*, Prentice-Hall, 2005.
- [8] B. Deal, “Standardized Terminology for Oxide Charges Associated with Thermally Oxidized Silicon,” *Journal of the Electrochemical Society*, vol. 127, no. 4, pp. 979–981, 1980.
- [9] T. Grasser, K. Rott, H. Reisinger, P. Wagner, W. Goes, F. Schanovsky, M. Waltl, M. Toledano-Luque, and B. Kaczer, “Advanced Characterization of Oxide Traps: The Dynamic Time-Dependent Defect Spectroscopy,” *Proc. Intl. Rel. Phys. Symp. (IRPS)*, pp. 2D.2.1–2D.2.7, 2013.
- [10] T. Grasser, H. Reisinger, P-J Wagner, F. Schanovsky, W. Gös, and B. Kaczer, “The Time Dependent Defect Spectroscopy (TDDS) for the Characterization of the Bias Temperature Instability,” *Proc. Intl. Rel. Phys. Symp. (IRPS)*, pp. 16–25, 2010.
- [11] M. J. Uren, M. J. Kirton, and S. Collins, “Anomalous Telegraph Noise in Small-Area Silicon Metal-Oxide-Semiconductor Field-Effect Transistors,” *Physical Review B*, vol. 37, no. 14, pp. 8346, 1988.
- [12] N. Sano, K. Matsuzawa, M. Mukai, and N. Nakayama, “Role of Long-Range and Short-Range Coulomb Potentials in Threshold Characteristics under Discrete Dopants in sub-0.1 μm Si-MOSFETs,” pp. 275–278, 2000.
- [13] K. Madsen, H.B. Nielsen, and O. Tingleff, “Methods for Non-linear Least Squares Problems,” Technical University of Denmark, 2004.
- [14] K. Meyberg and P. Vachenauer, *Höhere Mathematik 1: Differential-und Integralrechnung Vektor- und Matrizenrechnung*, Springer-Verlag, 2001.
- [15] T.K. Moon and W.C. Stirling, *Mathematical Methods and Algorithms for Signal Processing*, Prentice Hall, 2000.
- [16] “gnuplot documentation,” http://www.gnuplot.info/docs_4.0/gnuplot.html, accessed December 22, 2015.

-
- [17] W. H. Press, *Numerical Recipes 3rd Edition: The Art of Scientific Computing*, Cambridge university press, 2007.
- [18] J. A. Nelder and R. Mead, "A Simplex Method for Function Minimization," *The Computer Journal*, vol. 7, no. 4, pp. 308–313, 1965.
- [19] Global TCAD Solutions, "*Minimos-NT, User Manual*", 2015.
- [20] "Global TCAD Solutions homepage," <http://http://www.globaltcad.com>, accessed January 5, 2016.
- [21] Global TCAD Solutions, "*GTS Vision / Structure, User Manual*", 2015.
- [22] "Python Software Foundation. Python Language Reference, version 2.7," <http://www.python.org>, accessed January 4, 2016.
- [23] "Numpy and Scipy Documentation," <http://docs.scipy.org/doc/>, accessed January 6, 2016.
- [24] "scipy.optimize.fmin documentation," <http://docs.scipy.org/doc/scipy-0.15.1/reference/generated/scipy.optimize.fmin.html>, accessed January 5, 2016.
- [25] D. N. Joanes and C. A. Gill, "Comparing Measures of Sample Skewness and Kurtosis," *The Statistician*, pp. 183–189, 1998.
- [26] A. Körner, "VU Mathematik 3 f. ET, Wahrscheinlichkeitsrechnung und Statistik," *Lecture Notes*, 2014.